New highly radioactive particles derived from Fukushima Daiichi Reactor Unit 1 : Properties and environmental impacts

Morooka, Kazuya

2021-06-15

Morooka , K , Kurihara , E , Takehara , M , Takami , R , Fueda , K , Horie , K , Takehara , M , Yamasaki , S , Ohnuki , T , Grambow , B , Law , G T W , Ang , W L J , Bower , W R , Parker , J , Ewing , R C & Utsunomiya , S 2021 , ' New highly radioactive particles derived from Fukushima Daiichi Reactor Unit 1 : Properties and environmental impacts ' , The Science of the Total Environment , vol. 773 , 145639 . https://doi.org/10.1016/j.scitotenv.2021.145639

http://hdl.handle.net/10138/354576
https://doi.org/10.1016/j.scitotenv.2021.145639

Graphical abstract

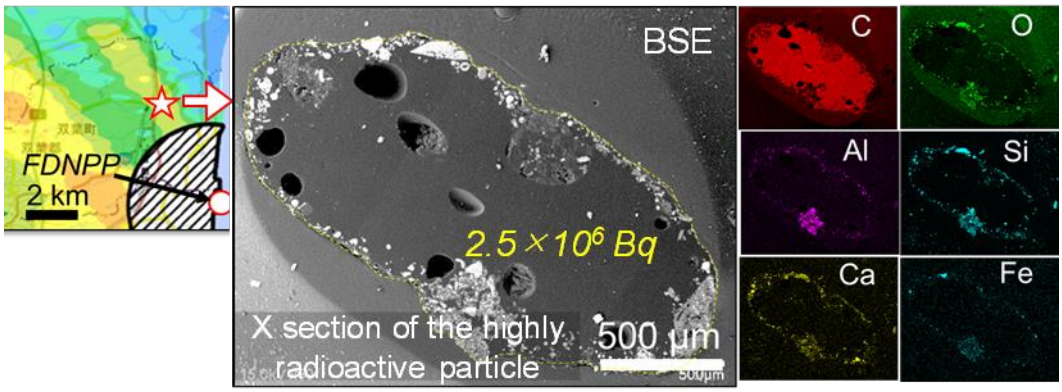

Highlights

- New type of radioactive particles discovered 3.9 km NNW of Fukushima Daiichi
- Particles consist of glassy carbon with other micro-particles embedded into the surface
- Isotopic analysis indicates volatilization of Cs before the H_2 explosion
- The human health effects of the particles are expected to be minimal owing to their large size (>500 μm)

Original manuscript submitted to *Science of the Total Environment* on October 23rd, 2020

Revision submitted on January 30, 2021

New Highly Radioactive Particles Derived from Fukushima Daiichi Reactor Unit 1: Properties and Environmental Impacts

Kazuya Morooka,[a] Eitaro Kurihara,[a] Masato Takehara,[a] Ryu Takami,[a] Kazuki Fueda,[a] Kenji Horie,[b,c] Mami Takehara,[b] Shinya Yamasaki,[d] Toshihiko Ohnuki,[e] Bernd Grambow,[f] Gareth T. W. Law,[g] Joyce W. L. Ang,[g] William R. Bower,[g] Julia Parker, [h] Rodney C. Ewing,[i] and Satoshi Utsunomiya,[a]*

[a]Department of Chemistry, Kyushu University, 744 Motooka, Nishi-ku, Fukuoka 819-0395, Japan

[b]National Institute of Polar Research, 10-3, Midori-cho, Tachikawa-shi, Tokyo 190-8518, Japan

[c]Department of Polar Science, The Graduate University for Advanced Studies (SOKENDAI), Shonan Village, Hayama, Kanagawa, 240-0193, Japan

[d]Faculty of Pure and Applied Sciences and Center for Research in Isotopes and Environmental

Dynamics, University of Tsukuba, 1-1-1 Tennodai, Tsukuba, Ibaraki 305-8577 Japan

[e]Laboratory for Advanced Nuclear Energy, Institute of Innovative Research, Tokyo Institute of Technology, 2-12-1 Ookayama, Meguro-ku, Tokyo 152-8550, Japan

[f]SUBATECH, IMT Atlantique, CNRS-IN2P3, the University of Nantes, Nantes 44307, France

[g]Radiochemistry Unit, Department of Chemistry, The University of Helsinki, Helsinki 00014, Finland

[h]Diamond Light Source, Harwell Science and Innovation Campus, Didcot OX11 0DE, UK

[i]Department of Geological Sciences and Center for International Security and Cooperation, Stanford University, Stanford, CA 94305-2115 USA

Email: utsunomiya.satoshi.998@m.kyushu-u.ac.jp

Abstract

A contaminated zone elongated toward Futaba Town, north-northwest of the Fukushima Daiichi Nuclear Power Plant (FDNPP), contains highly radioactive particles released from reactor Unit 1. There are uncertainties associated with the physio-chemical properties and environmental impacts of these particles. In this study, 31 radioactive particles were isolated from surface soils collected 3.9 km north-northwest of the FDNPP. Two of these particles have the highest particle-associated $^{134+137}$Cs activity ever reported for Fukushima (6.1×10^5 and 2.5×10^6 Bq per particle after decay-correction to March, 2011). The new, highly-radioactive particle labeled FTB1 is an aggregate of flaky silicate nanoparticles with an amorphous structure containing ~0.8 wt% Cs, occasionally associated with SiO_2 and TiO_2 inclusions. FTB1 likely originates from the reactor building, which was damaged by a H_2 explosion, after adsorbing volatilized Cs. The $^{134+137}$Cs activity in the other highly radioactive particle labeled FTB26 exceeded 10^6 Bq. FTB26 has a glassy carbon core and a surface that is embedded with numerous micro-particles: Pb−Sn alloy, fibrous Al-silicate, Ca-carbonate or hydroxide, and quartz. The isotopic signatures of the micro-particles indicate neutron capture by B, Cs volatilization, and adsorption of natural Ba. The composition of the micro-particles on FTB26 reflects the composition of airborne particles at the moment of the H_2 explosion. Owing to their large size, the

health effects of the highly radioactive particles are likely limited to external radiation during static contact with skin; the highly radioactive particles are thus expected to have negligible health impacts for humans. By investigating the mobility of the highly radioactive particles, we can better understand how the radiation dose transfers through environments impacted by Unit 1. The highly radioactive particles also provide insights into the atmospheric conditions at the time of the Unit 1 explosion and the physio-chemical phenomena that occurred during reactor meltdown.

50 **Keywords**

51 Radioactive particle, Unit 1, Fukushima Daiichi Nuclear Power Plant, cesium, boron, isotopic analysis

1. Introduction

The great east Japan earthquake, which occurred in March, 2011, was followed by a tsunami that hit the Fukushima Daiichi Nuclear Power Plant (FDNPP), causing a power outage and meltdowns in three reactors. Subsequently, a large-scale corium (a mixture of melted nuclear fuels and fuel assembly materials) formed in Units 1 and 3. Before melting, the fuel rods experienced temperatures >2200℃ and interacted with vaporized water, generating hydrogen by the reaction: $Zr + 2H_2O \rightarrow ZrO_2 + 2H_2$. Catastrophic hydrogen explosions then occurred in the reactor buildings (IAEA, 2015; Iwata et al., 2012a). During the meltdowns, the corium broke through the reactor pressure vessel (RPV) and dropped onto the concrete pedestal of the primary containment vessel (PCV). The molten core–concrete interaction (MCCI) generated radioactive aerosols (Furuki et al., 2017). The corium was further mixed with various structural materials, forming fuel debris upon cooling (IAEA, 2015). During the hydrogen explosion and/or venting events, ~5.2×10^{17} Bq of various radionuclides, including 10^{15}–10^{16} Bq of $^{134+137}$Cs, were released into the environment (Buesseler et al., 2017; Chino et al., 2011; Koo et al., 2014; Steinhauser et al., 2014). Radioactive ^{137}Cs and ^{134}Cs, with half-lives of 30.2 and 2.1 years, respectively, have largely contributed to the present high radiation dose in Fukushima Prefecture and its vicinity. The released Cs includes water-soluble Cs and two types of sparingly soluble Cs. The water-soluble forms

68 of Cs, such as CsI and CsOH, were mostly precipitated with rainwater and then the dissolved Cs
69 ions absorbed onto clay minerals and other geomedia in the surface soil (Auvinen et al., 2000; Iwata
70 et al., 2012b; Kaneko et al., 2015). The sparingly soluble Cs exists as fine particles and is classified
71 into two types based on different physical and chemical properties (Ikenoue et al., 2020).

72 To clarify the terminology, “Cs-rich” micro-particles (CsMPs) are defined as micro-
73 particles with dimensions of several micrometers with a bulk composition that includes O, Si, Zn, Fe,
74 and Cs. The Cs concentration in CsMPs (~10^{11} Bq/g) can be detected by scanning electron microscopy
75 with energy-dispersive X-ray spectroscopy (SEM−EDX) (Furuki et al., 2017). In this sense, the CsMP
76 is not simply a Cs-bearing micro-particle. After decay-correction to March 12 of 2011, the $^{134}Cs/^{137}Cs$
77 radioactivity ratio of CsMPs exceeds 1.0, which is close to the average radioactivity ratios in Units 2
78 and 3 (1.08 and 1.05, respectively (Nishihara et al., 2012)). In contrast, the ratio is less than 1.0 for the
79 radioactive particles released from Unit 1 (calculated ratio is 0.945 (Nishihara et al., 2012)). Based on
80 this difference, the radioactive particles emitted by the damaged FDNPP reactors have been classified
81 into two groups: (i) particles derived from either Unit 2 or 3, which are defined as CsMPs (Furuki et
82 al., 2017), and (ii) particles released from Unit 1. The CsMPs occasionally contain nano-scale
83 inclusions composed of fission-fragment radionuclides, structural materials, and debris fragments

84 (Furuki et al., 2017; Imoto et al., 2017; Ochiai et al., 2018). Many CsMPs were transported by Cs-rich
85 plumes over long distances (>200 km from the FDNPP) (Ikehara et al., 2020; Nakajima et al., 2017;
86 Tsuruta et al., 2015; Utsunomiya et al., 2019). The CsMPs deposited on the ground have high
87 chemical durability, similar to that of Si-based glass (Suetake et al., 2019), and remain with various
88 radioactive fractions of CsMPs in the total $^{134+137}$Cs activity (Ikehara et al., 2020, 2018).
89 Meanwhile, the sparingly soluble micro-particles of the present study are distributed in an
90 elongated zone extending north-northwest from the FDNPP. This narrow zone is contaminated mainly
91 by radionuclides released from Unit 1 (Fig. 1). The radionuclides were released by the hydrogen
92 explosion that occurred on March 12 of 2011, and were spread by the prevailing winds at that time
93 (Katata et al., 2012). The explosion at Unit 1 blew out the side wall of the fifth floor, causing collapse
94 of the ceiling. The ejecta were released horizontally at an approximate height of 50 m (Nomura, 1969;
95 TEPCO, 2017). Consequently, large particles were deposited along a north-northwest direction over a
96 short period, forming a highly-contaminated, linear zone (Fig. 1).
97 The ^{134}Cs/^{137}Cs activity ratio in these radioactive particles is 0.94 on average (Satou et al.,
98 2018), consistent with the average ratio in Unit 1 (Nishihara et al., 2012). The dispersed particles are
99 much larger (diameter 70–400 μm) than CsMPs, and their shapes are spherical, angular, or fibrous

100 (Martin et al., 2020, 2017; Satou et al., 2018). Although the $^{134+137}$Cs activity of each particle is high,
101 the $^{134+137}$Cs activity per unit mass (~10^6 Bq/g) is lower than in CsMPs, and the Cs cannot be detected
102 by EDX. The low Cs concentrations can be detected by gamma spectroscopy or synchrotron micro-X-
103 ray fluorescence (μ-XRF) (Martin et al., 2019; Ono et al., 2017). The main composition of the sparingly
104 soluble micro-particles (O, Si, Al, Zn and Fe) is similar to that of CsMPs except for the Al-content,
105 which is much higher in the Unit-1 radioactive particles than in CsMPs. Some of the particles has been
106 shown to have a fibrous texture, and have been inferred to originate from the insulating materials used
107 in the reactor building (Martin et al., 2017). Further, the uranium isotope ratio, ^{235}U/^{238}U, from another
108 Unit-1 radioactive particle was reported to be 0.0354 ± 0.0015 (Martin et al., 2019), comparable to the
109 uranium isotope ratios in Unit 1 (Nishihara et al., 2012). Because the physio-chemical properties
110 (composition, size, texture, and radioactivity) of the FDNPP contaminants are highly variable, the
111 conditions during the accident and the environmental impacts of the released particles remain obscure
112 and further study is clearly needed.

113 Reflecting the above, in the present study, we isolated 31 radioactive particles from the
114 surface soils of the area impacted by Unit 1. The hypotheses considered in our research were: (i) there
115 should be radioactive particles released from Unit 1 with much higher $^{134+137}$Cs activities than that

described in the current literature, and their environmental impacts need to be evaluated based on their physio-chemical properties; (ii) these radioactive particles retain evidence of conditions inside the reactors / reactor buildings at the time of explosion.

Two of 31 particles examined emitted extremely high levels of $^{134+137}$Cs activity (>10^5 Bq per particle). Radioactive particles with such a high activity have been discovered at various locations where accidents and radioactive releases occurred, and such materials have been characterized using a variety of standard and state-of-the-art micro-analytical techniques (*e.g.*, Byrnes et al., 2020; Eriksson et al., 2005; IAEA, 2011 and references therein; Salbu et al., 2001). Until now, they have not been noted in areas impacted by FDNPP contamination. Here, through use of rigorous micro-scale analyses, we elucidate the specific physio-chemical properties of the new highly radioactive particles, adding to our understanding of the FDNPP and meltdown conditions at the time of the Unit-1 hydrogen explosion. The potential health effects of the contaminant particles are also discussed. This work is of particular importance because the environmental remediation in the vicinity of FDNPP and decommissioning of the damaged reactors are ongoing and will last for decades. Any new information pertaining to the distribution, abundance, type, and composition, of FDNPP-derived radioactive particles can inform both of these endeavors (*e.g.*, improve worker safety and guide clean-up / decommissioning strategies.).

132

133 **2. Sampling and Methods**

134 2.1. Sample description

135 The sampling campaign was conducted on December 10, 2017 and July 26, 2018. The
136 sampling area was Futaba Town in Fukushima Prefecture. Surface soils were collected from the top ~1
137 cm of ground surface at four sampling sites. Among the 31 radioactive particles isolated from the soils,
138 two particles labeled as FTB1 and FTB26 were highly radioactive emitting $^{134+137}$Cs activity above 10^5
139 Bq. Both particles were separated from soils located approximately 3.9 km north-northwest of the
140 FDNPP (see Fig. 1).

141

142 2.2. Isolation of radioactive particles

143 The radioactive particles were separated from the soils as described in our previous study
144 (Furuki et al., 2017). Their locations were determined by an autoradiography technique (Fig. S1). First,
145 an imaging plate (Fuji film, BAS-SR 2025) was placed in contact with the soils. The plate exposure
146 time was 15 minutes (shorter if the activity was very high). Autoradiograph images with pixel sizes of
147 50–100 μm were recorded by an imaging-plate reader (Fuji film, FLA-5000). The positions of intensely

148 radioactive spots were identified and droplets of pure water were added to these spots. The water
149 droplets were then drawn with a pipette, forming suspensions containing small amounts of soil particles.
150 This procedure was repeated until the suspension contained negligible amounts of soil particles. In
151 contrast to CsMPs, which are isolated using pieces of double-stick carbon tape, the radioactive particles
152 derived from Unit 1 were sufficiently large for hand-picking. Therefore, they were picked up with
153 tweezers and placed on the double-stick carbon tape.
154
155 2.3. Scanning Electron Microscopy (SEM)
156 Prior to SEM analysis, the isolated radioactive particles were coated using a carbon coater
157 (SANYU, SC-701C, Tokyo, Japan). The particles were then analyzed by SEM (HITACHI, SU3500 and
158 SU6600, Tokyo, Japan) equipped with EDX (EDAX Genesis, NJ, USA). The acceleration voltages were
159 set to 5–25 kV for surface morphology imaging and 15–25 kV for elemental analyses (area analysis and
160 elemental mapping).
161
162 2.4. X-ray fluorescence spectroscopy (XRF)
163 The FTB26 sample was subjected to XRF elemental mapping using an X-ray analytical

164 microscope (XGT5000, HORIBA, Tokyo, Japan). The acceleration voltage and X-ray beam diameter
165 were 50 kV and 100 μm, respectively. The scan width and speed were 4.096 mm and 100 s/frame,
166 respectively, and each frame was composed of 512 × 512 pixels.
167
168 2.5. Three-dimensional Visualization
169 The FTB26 sample was visualized by three-dimensional (3D) X-ray tomography using a
170 high-resolution 3D X-ray computed tomography (CT) system (Bruker, SKYSCAN1172, Kontich,
171 Belgium). The tilt ranged from 0° to 196° at 0.7°-intervals. The pixel resolution was ~0.8 μm. The 3D
172 structure was reconstructed using Amira (Maxnet) and TEMography (System in Frontier) software.
173
174 2.6. Preparation of cross-sectional specimen
175 One of the highly radioactive particles (FTB26) was fixed on a glass slide with epoxy
176 adhesive (Nichiban, Nagoya, Japan). The fixed particle was carefully cut by a 0.1 mm-thick diamond
177 blade (Maruto, Tokyo, Japan). The cut surface was polished using a tripod polishing system (PELCO
178 Tripod Polisher 590, Ted Pella, CA, USA) with a diamond slurry. As the polishing progressed, the gain
179 size of the slurry was reduced in steps until the final size was <~1 μm.

180

181 2.7. Transmission electron microscopy (TEM)

182 High-resolution TEM (HRTEM) with EDX and high-angle annular dark-field scanning
183 transmission electron microscopy (HAADF–STEM) were performed using a JEOL JEM-ARM200F
184 (Tokyo, Japan) with an acceleration voltage of 200 kV. The STEM–EDX mapping was controlled by
185 JOEL Analysis Station software. To minimize the effects of sample drift, the elemental map was
186 acquired in drift-correction mode. The STEM probe size was ~0.13 nm, generating ~140 pA of current
187 after inserting a condenser lens with a 40-μm aperture. During the data collection, the angle of the
188 HAADF detector ranged over ~97–256 mrad. Electron energy-loss spectroscopy (EELS) was completed
189 in dual EELS mode with an entrance aperture of 25 mm, a dispersion of 2.5 eV/ch, and a collection half
190 angle of β =11.3 mrad. The FWHM of the zero-loss peak was ~1 eV.

191 Thin foils were prepared from the highly radioactive particles by a focused ion beam (FIB)
192 system (FEI, Quanta 3D FEG 200i Dual Beam, MA, USA). The primary ion source was gallium and
193 the foils were deposited with tungsten to minimize radiation damage by ion bombardment. The current
194 and accelerating voltage of the ion beam were adjusted to 49 pA–30 nA and 8–30 kV, respectively,
195 depending on the thinning progress and sample properties (such as hardness and size). Each thinned

196 piece was attached to a convex-shaped Cu grid (Omniprobe FIB Lift-Out grid) in order to cut by the
197 FIB and was further thinned by an ion beam operated at 8 kV.
198
199 2.8. Gamma Spectrometry.
200 The ^{134}Cs and ^{137}Cs activities of FTB1 and FTB26 were determined by gamma spectrometry.
201 The measurements were conducted using Ge semiconductor detectors GMX35 and GMX40 (SEIKO
202 E&G, Tokyo, Japan) at the Center for Radioisotopes in Kyushu University, Japan. The $^{134+137}$Cs activity
203 of an additional micro-particle of size ~400 μm was precisely determined at the radioisotope center in
204 the University of Tsukuba. To eliminate the effects of peak summation for ^{134}Cs, the peak at 604 keV
205 was precisely measured to obtain the detection efficiency using a ^{134}Cs standard solution sample that
206 was purchased from the Japan Radioisotope Association (product CZ010). Following a previous study
207 (Furuki et al., 2017), this micro-particle was employed as the in-house standard point specimen for ^{134}Cs
208 and ^{137}Cs. As of March 12, 2011, the ^{134}Cs and ^{137}Cs activities of the point source standard were
209 determined to be 110 and 105 Bq, respectively. In analysis of the highly radioactive particles, dead-time
210 correction was employed to deduce the live-time count rate of gamma ray in the software, Gamma
211 Studio (SEIKO E&G).

212

213 2.9. Secondary ion mass spectrometry (SIMS)

214 The isotopic ratios in FTB26 on the surface and the prepared cross-sectional specimen were
215 analyzed using SIMS (SHRIMP-II, Australian Scientific Instruments) at the National Institute of Polar
216 Research, Tokyo. Prior to analysis, both the surface and cross section were coated with a 13.5 nm-thick
217 Au layer. The FTB26 surface was sputtered with an O_2^- primary ion beam with a current of 5.30–6.87
218 nA and a beam diameter of ~25 μm. The typical mass resolution ($M/\Delta M$ at 1% peak height) was ~4,500
219 in the Cs–Ba-isotope analysis and ~3,000 in the B-isotope analysis. The mass calibration and standard
220 specimen for quantification accorded with the National Institute of Standards and Technology (NIST)
221 SRM612. The $^{10}B^+$ and $^{11}B^+$ masses were scanned in the B-isotope analysis, and masses of 133, 134,
222 135, 137, and 138 were scanned in the Cs–Ba-isotope analysis. Note that isotopic interferences occur
223 between the Cs and Ba ions at masses 134, 135, and 137.

224

225 2.10. Nano-focus Synchrotron XRF and XRD

226 Nano-focus XRF and XRD measurements was performed at the Diamond Light Source I14
227 beamline in the U.K. A thin foil (FTB1-A) was extracted from sample FTB1 using FIB milling (see

228 section 2.7) and mounted on a convex-shaped Cu grid (Omniprobe FIB Lift-Out grid), and then placed
229 in double Kapton containment for radiological safety. XRF data from the thin foil was collected in
230 backscatter mode using a ~50 nm (horizontal) beam spot (horizontally reflecting double-crystal
231 monochromator) and a Rayspec^{TM} 4 element Si drift detector (0.6-0.8 sr solid angle). XRF mapping
232 was performed with an incident beam energy of 6.0 keV and 19.0 keV. XRF maps were fitted,
233 background subtracted, and plotted for publication using PyMCA (Solé et al., 2007). Nano-focus XRD
234 maps were collected with an Excalibur 3M detector (Marchal et al., 2013). The sample to detector
235 distance was 366 mm (calibrated using a CeO_2 standard), the beam spot was as per XRF data collection,
236 and the incident beam energy was 19.0 keV. Diffraction patterns from each scan position were converted
237 from 2D images to 1D spectra using DAWN for azimuthal integration before subtracting a polynomial
238 background function (Filik et al., 2017). The diffraction patterns were summed across the mapped area
239 to give a representative pattern.
240
241 **Results**
242 3.1. ^{134}Cs and ^{137}Cs activities
243 Thirty-one radioactive particles were isolated from soils collected at four locations in Futaba

Town (Fig. 1, Table S1). The ^{134}Cs and ^{137}Cs activities of these particles after decay-correction to March 12, 2011, are given in Table 1. Figure 2 plots the $^{134}Cs/^{137}Cs$ activity ratio of the particles versus the ^{137}Cs activity on a logarithmic scale. For comparison, the $^{134}Cs/^{137}Cs$ activity ratios of CsMPs reported in previous studies (Furuki et al., 2017; Imoto et al., 2017; Kurihara et al., 2020; Ochiai et al., 2018; Suetake et al., 2019) are also plotted, along with the average $^{134}Cs/^{137}Cs$ activity ratios in Unit 1 (0.945), Unit 2 (1.08), and Unit 3 (1.05) calculated using ORIGEN-II code with JENDL data (Nishihara et al., 2012). The $^{134}Cs/^{137}Cs$ activity ratios in the CsMPs were close to the calculated average ratios in Units 2 and 3; whereas, those of the particles in the present study are a good match for the average ratio in Unit 1. This result confirms that the isolated particles in the present study were derived from Unit 1. The ^{137}Cs activity of most of the particles in the present study ranged from 10^0 to 10^3 Bq, but the two particles designated FTB1 and FTB26 showed extremely high ^{137}Cs activities (3.1×10^5 and 1.3×10^6 Bq, respectively; see Table 1). The total $^{134+137}Cs$ activities of FTB1 and FTB26, 6.1×10^5 and 2.5×10^6 Bq, respectively, far exceed the highest reported $^{134+137}Cs$ activity per particle (3.7×10^4 Bq) released from the FDNPP (Martin et al., 2020). For this reason, the following results and discussion focus on these two new highly radioactive particles, FTB1 and FTB26. The activities and SEM results of the other 29 particles are given in the Supplementary Information (Fig. S2, Table S2).

260

261 3.2. FTB1

262 Figure 3a is a secondary electron (SE) SEM image of FTB1 associated with the elemental
263 maps of the major elements. The particle is angular with an approximate size of 300 μm. From the EDX
264 spectrum (Fig. 3b), the main elements were identified as O, Al, and Si. Ca and Fe are distributed
265 heterogeneously on the particle surface. A small Cs peak was detected over the entire surface of the
266 specimen (Fig. 3b). This sample, with a sufficiently high Cs content (>0.1 wt.%), is the first Unit 1-
267 derived particle with a recognizable Cs peak in SEM–EDX spectroscopy. The particle was subsequently
268 crushed into smaller pieces using tweezers for a detailed internal analysis. The SE image and elemental
269 maps of the separated particles are shown in Fig. S3a. Calcium and Fe were heterogeneously distributed
270 on the fractured surfaces. In an EDX point analysis of the micro-particles that adhered to the surface,
271 Cs was associated with aluminosilicate, and calcium sulfate was also present (Fig. S3b). Presence of
272 calcium sulfate micro-particles was further supported by enlarged elemental maps that reveal a
273 correlation between Ca and S (Fig. S3c).

274 Two TEM thin foils (FTB1-A and FTB1-B) were successfully prepared from a FTB1
275 fragment using the FIB system (Fig. S4). Panel (a) of Fig. 4 shows the HAADF–STEM image and

276 elemental maps of the major constituents of foil FTB1-A. The particle contained aggregations of flaky
277 nano-textures and numerous nano-pores (Fig. 4a). The matrix part was mainly composed of O, Si, Al,
278 and Fe, with trace K, Ca, Ti and Cs (EDX1 in Fig. 4a). The Cs content in the matrix (calculated as Cs_2O)
279 was semi-quantitatively determined as ~0.83 wt.% on average (Table 2). Selected area electron
280 diffraction (SAED) patterns revealed diffuse diffraction maxima confirming an amorphous structure
281 (Fig. 4a), which is also supported by nano-focus X-ray diffraction analysis of FTB1 (Fig. S5a). FTB1-
282 A also contained titanium oxides with trace Zr, in which Cs was absent (EDX2 in Fig. 4a). Nano-focus
283 X-ray analysis of FTB1 also confirmed that the Ti-oxides were associated with trace Zr and absent with
284 Cs (Fig. S5). The structure and composition of FTB1-B were similar to those of FTB1-A (Fig. 4b): flaky
285 texture, pores, and diffuse diffraction maxima. The average Cs content in the FTB1-B matrix (calculated
286 as Cs_2O) was determined as ~0.68 wt.%. SiO_2-rich inclusions, in which no Cs was detected, also
287 presented in the matrix (EDX4 Fig. 4b). Thus, the Cs in FTB1 was mainly associated with
288 aluminosilicate.
289
290 3.3. FTB26
291 Figure 5 shows the SE image and elemental map of the major elements in FTB26. This

292 sample was also angular in shape with an approximate diameter of 3 mm (Fig. 5a). Enlarged SE images
293 revealed numerous spherical and fibrous micro-particles attached to the surface (Fig. 5b and c). The
294 elemental map confirmed the distributions of Si, O, and Na on the fibrous and spherical particles. The
295 host particle was dominated by carbon, although FTB26 was not carbon-coated prior to SEM
296 observation (Fig. 5b). According to the EDX spectra collected from the points labeled EDX 1–3 in Fig.
297 5b and c, the fibrous and spherical particles attached on the surface contained Si as a dominant
298 constituent, and trace amounts of Ca, Fe, and Pb (Fig. 5d).

299 XRF mapping of FTB26 was performed by scanning the X-ray analytical microscope over
300 the entire particle (Fig. 6a). Note that the contrast does not represent the relative concentration between
301 the elements, because it depends on the energy of the incident X-ray beam and the fluorescence
302 efficiency. The maps show that Ti, Fe, and Zn were heterogeneously distributed as discrete particulates
303 over the entire particle. At one spot, Cu was associated with Fe. The X-ray CT image of FTB26 indicated
304 high-density particles at the surfaces (Supporting Information, movie S1). A sequence of cross-sectional
305 CT images sliced at constant intervals also revealed a dense rim and a less dense core, with many pores
306 as large as several hundreds of micrometers across (Fig. 6b).

307 A cross section specimen was also prepared (Fig. S6a and b). Several pores appeared within

308 the particle in a back-scattered electron (BSE) image, consistent with the CT images (Fig. 7a). The
309 elemental maps revealed a carbon core and a rim with heterogeneous distributions of other elements
310 such as Si, Al, Fe, Na, Ti, Mg, and Ca (Fig. 7a). The purity of the carbon core was confirmed in the
311 EDX spectrum EDX1 (Fig. 7b). An enlarged image and the elemental maps of the rim (enclosed within
312 the dotted yellow-edged rectangle in Fig. 7a) revealed numerous fine particles composed mainly of
313 silicate, along with Na, Mg, Al, and Ca. Iron was also present with a different distribution. As clarified
314 in the elemental map, these particles are embedded within the carbon matrix rather than attached on the
315 surface.

316 The individual fine particles embedded within the rim of FTB26 were characterized in detail
317 by SEM (Fig. 8). Figure 8a shows the BSE image of a rim associated with elemental maps and the EDX
318 spectra collected from the points labeled EDX1–6. The maps reveal a silicate phase-bearing Al, Ca ±
319 Na, Pb–(Cr–Zn–O) phase, Ca–(C–O) phase, and Fe–Cr–O phase. Most of these phases were <50 μm
320 in size and embedded in the carbon core. The Fe–Cr–O phase (represented by EDX1) was dominated
321 by Fe oxides with trace Cr (Fe/Cr molar ratio = 7.8). The particle indicated by EDX2 was primarily Pb
322 with small amounts of Si and O and negligible Cr and Zn, indicating a probable composition of Pb metal
323 with X-ray emission from the surrounding silicate induced by propagation of electrons near the sample

surface, as evidenced in the Si and O elemental maps. However, a Pb-oxide composition cannot be excluded. The micro-particle labeled EDX3 was predominantly Ca, in the form of calcium carbonate or calcium hydroxide. Meanwhile, EDX4 was composed of silicate with Ca. The phase was difficult to identify based on composition alone. The micro-particle labeled EDX5 was most likely composed of SiO_2 (quartz). The particle indicated by EDX6 was also silicate with a composition similar to that of Na-rich glass.

Figure 8b shows the SE image, an enlarged SE image, the elemental maps, and EDX spectra collected from the micro-particles at the rim of the carbon core. The micro-particle indicated by EDX7 was composed of Fe–Zn–oxides with an Fe/Zn molar ratio of ~3.9. The enlarged SE image revealed a Pb–Sn alloy, which was confirmed in the EDX spectrum (EDX8). In a semi-quantitative area analysis of the whole particle, the Pb:Sn molar ratio was deduced as 58:42. However, the elemental maps clarified that Sn and Pb were chemically separated within the particle. The particle indicated by EDX9 was aluminosilicate with Ca and S and was seemingly a mixture of clay-like aluminosilicate and calcium sulfate. A BSE image of another rim part presented angular particles of approximate size (200 × 100) μm^2, and main compositions of Si and O with Ca and Na-like glassy material (Fig. 8c). Figure 8d is an SE image of a Pb metal particle (EDX11). A BSE image of another embedded particle and its elemental

340 map showed an aggregate of numerous particles of a few microns in size. The image displays a fractured
341 texture and the fractured particles were surrounded by a carbon matrix. Semi-quantitative EDX analysis
342 of the entire aggregate (EDX12) revealed Al and Si as the dominant constituents (Al + Si > 71 wt%),
343 with trace Ca, Na, Mg, and Fe. In the elemental maps, the Si, Al, and O were uniform; whereas, Ca, Mg,
344 Na, and Fe were heterogeneously distributed within the aggregate. An SE image and corresponding
345 elemental maps of another part of the rim revealed similar occurrences of various particles, including a
346 Ca phase, immiscible Pb–Sn metal particles, and a silicate phase. The Si phase was identified as SiO_2
347 (quartz) (EDX13).
348 The carbon core of FTB26 was further investigated after FIB sectioning of the part indicated
349 by the arrow in Fig. 7a. The HAADF–STEM image showed a uniform structure without any inclusions
350 (Fig. 9a). A representative SAED pattern was collected from the area enclosed by the yellow-edged
351 circle in Fig. 9a. The diffuse diffraction maxima in the SAED pattern indicates an amorphous structure
352 (Fig. 9a insert). The representative EDX spectrum revealed a pure carbon core, consistent with the SEM
353 observations. The EELS spectrum of the carbon showed two absorption peaks derived from σ* and π*
354 antibonding orbitals (Fig.9c), indicating that the FTB26 matrix was amorphous carbon forming σ and
355 π bonds. Given its transparency (Fig. S6b), the carbon core was tentatively identified as glassy carbon

356 (Yao et al., 2014; Zeng et al., 2017).

357 The boron isotope ratio $^{11}B/^{10}B$ at the FTB26 surface ranged from 4.14 to 4.28 (average =

358 4.18, $n = 5$) (Table 4a). To obtain the average ratio, five analytical spots were arbitrarily selected on the

359 surface as shown in Fig. S6c. At all analytical points, the $^{11}B/^{10}B$ isotopic ratio was slightly higher on

360 FTB26 than on SRM612 (4.049) and that of the natural isotope ratio (4.044; Foster et al., 2016)),

361 indicating that ^{10}B had been consumed through neutron absorption of ^{10}B, namely, $^{10}B(n,\alpha)^{7}Li$. The B

362 concentration, deduced by comparison with NIST standard SRM612, ranged from 5 to 6625 ppm. Boron

363 was below the detection limit in the carbon core of the cross-sectional sample; hence, the data are not

364 given in Table 4a. The cesium isotope distribution was investigated by measuring ^{133}Cs. The ion counts

365 (cps) were almost nil inside the core but reached ~ 19000 at the rim (Table 5a, Fig.10a). Hence, the

366 subsequent analysis focused on spots 3–8 around the rim. The ion-count ratio of mass-135/mass-133

367 represents the $(^{135}Cs+^{135}Ba)/^{133}Cs$ ratio due to isotopic interference between ^{135}Cs and ^{135}Ba. The

368 measured ratios ranged from 0.49 to 1.2, slightly higher than that in Unit 1 (Nishihara et al., 2012) (Fig.

369 10b). Similarly, $(^{137}Cs+^{137}Ba)/^{133}Cs$ ranged from 0.99 to 2.2, slightly higher than in Unit 1 (Fig. 10c).

370 Meanwhile, $(^{134}Cs+^{134}Ba)/^{138}Ba$ ranged from 0.037 to 0.044, much lower than in Unit 1 (Fig. 10d). The

371 ion-count ratio of mass-135/mass-137, given by $(^{135}Cs+^{135}Ba)/(^{137}Cs+^{137}Ba)$, was nearly constant

372 around ~0.5, which is higher than the calculated ratio in Unit 1 (Nishihara et al., 2012).

373

374 **4. Discussion**

375 4.1. Specific physico-chemical properties and isotopic signature of the new highly radioactive particles

376 The total Cs activities of FTB1 and FTB26 were 6.1×10^5 and 2.5×10^6 Bq, respectively,

377 higher than that measured for any other radioactive particles derived from Unit 1 (Fig. 2) (Martin et al.,

378 2020, 2019, 2017). These two highly radioactive particles exhibited different physio-chemical

379 properties. FTB1 consisted of aggregated submicron-sized aluminosilicates with a flaky texture and a

380 relatively high Cs content (detectable by EDX spectroscopy). In previous studies, the Cs occurrence in

381 all radioactive particles released from Unit 1 (besides CsMPs) were identifiable only through

382 synchrotron-radiation μXRF spectroscopy. Thus, the Cs concentration in FTB1 is considered to be high

383 even at <1 wt%. Although the origin of FTB1 is uncertain, aluminosilicates can be sourced from several

384 locations in the reactor building. One possible origin is the insulating material at the exterior of the RPV

385 (Martin et al., 2020, 2017). In FTB1, this source is unlikely because the nano-texture was compacted

386 and dense in the TEM image. Another possible source is a structural component, for example, a wall.

387 Although the source material cannot be specified conclusively, the radioactive Cs was uniformly

388 distributed within the aluminosilicate, evidence that a volatilized Cs species was likely adsorbed onto
389 the aluminosilicates before the Unit's hydrogen explosion. That is, the volatilized Cs had escaped from
390 the RPV before the hydrogen explosion at 15:36 on March 12 of 2011. There is a possibility that the
391 high Cs concentration is a result of adsorption of Cs after wet deposition during rain; however, the
392 $^{134+137}$Cs activity of FTB1 and FTB26 is abnormally high as compared with all other particles, such as
393 clays in soil, indicating that the radioactive Cs in the highly radioactive particles is unlikely to be the
394 results of post-depositional adsorption of Cs.

395 Unlike FTB1, FTB26 consisted of a mainly glassy carbon core with mixed π and σ bonds.
396 Numerous fine particles were embedded in the surface around the carbon core. Based on the SIMS
397 analysis, only these fine surface particles are associated with Cs and B. No significant Cs and B contents
398 were found in the glassy carbon core; thus, the core is non-radioactive. The high concentration of surface
399 B (up to ~6625 ppm) indicates that the B content is not of natural origin, but instead derived from the
400 high concentration of volatilized B species in the ambient atmosphere inside the reactor at the time of
401 the explosion. This conclusion is supported by the slightly higher ^{11}B/^{10}B isotopic ratio (4.13–4.27) than
402 in SRM612 (4.049). This elevated ratio confirms the neutron capture of ^{10}B, meaning that B likely
403 originated from B_4C in the control rods as predicted by experimental studies (Miwa et al., 2020, 2016).

On March 12 of 2011, a mixture of sea water with boric acid was injected into the Unit 1 reactor in a ratio of 20:45, after the hydrogen explosion on the same day (IAEA, 2015). Hence, the B detected in FTB26 could not be derived from the injected borate water.

Based on the Cs and Ba isotopes concentrated in the rim of FTB26, the ion-count ratios of (^{135}Cs + ^{135}Ba)/^{133}Cs and (^{137}Cs + ^{137}Ba)/^{133}Cs were slightly higher than the isotope ratios calculated for Unit 1, despite the lower ionization efficiency of Ba than of Cs in the SIMS analysis (Imoto et al., 2017). In CsMPs, the volatilized Cs was captured during their formation, so the ion-count ratios correspond to the ratios of the initial Cs isotopes of averaged fuel composition of their source reactor. In contrast, the ratios in the present study reflect the incorporation of the natural Ba isotopes ^{135}Ba and ^{137}Ba, indicating that a small amount of naturally occurring Ba was either volatilized inside the reactor building during the meltdown or adsorbed onto the particle surface after it was released to the environment. The amount of volatilized Ba in the reactor should be negligible considering the lower volatility of Ba as compared with Cs (Pontillon et al., 2010). A previous study also reported that almost no Ba was volatilized during meltdowns in FDNPP (Imoto et al., 2017). In addition, the natural abundance of Ba in upper continental crust is about 670 ppm (Hans Wedepohl, 1995), which is several orders of magnitude higher when compared to the concentration of radioactive Cs in the soil that contained FTB1 and 26 (7.8×10^6 Bq/kg

420 / 2.3 ppb of $^{134+137}$Cs). As a consequence, Ba detected in the FTB26 is most likely natural Ba adsorbed
421 after the particle was deposited in the environment.
422 Meanwhile, limited amounts of volatilized Cs were adsorbed on the surfaces of the
423 embedded micro-particles or the carbon core. In fact, the Cs concentrations were below the detection
424 limit of the EDX analysis. This finding strongly suggests that the timing and compositions of the
425 ambient atmosphere differed during the formation of FTB26 and CsMPs. The ion-count ratio (^{134}Cs +
426 ^{134}Ba)/^{138}Ba ranged from 0.03 to 0.04 in FTB26 (less than half that in Unit 1), but exceeded 100 in
427 CsMPs (Imoto et al., 2017). The ratios measured in the present study were very close to the ^{134}Ba/^{138}Ba
428 isotopic ratios of natural abundance, namely, 0.0337 (Eugster et al., 1969), strongly indicating the
429 occurrence of natural Ba. In addition, the ion-counts ratio (^{135}Cs + ^{135}Ba)/(^{137}Cs + ^{137}Ba) at the rim of
430 FTB26 ranged from 0.48 to 0.53; this is clearly higher than the (^{135}Cs + ^{135}Ba)/(^{137}Cs + ^{137}Ba) isotopic
431 ratio calculated in Unit 1 (0.365), and rather close to the natural abundance ^{135}Ba/^{137}Ba isotopic ratio of
432 0.619 (Eugster et al., 1969). Therefore, the ion-count ratio measured in the present study probably
433 reflected the isotopic ratio of natural Ba. The ion-count ratio (^{135}Cs + ^{135}Ba)/(^{137}Cs + ^{137}Ba) showed a
434 greater deviation from the natural Ba-isotope ratio toward the calculated ratio in Unit 1 than the (^{134}Cs
435 + ^{134}Ba)/^{138}Ba ratio, likely because the amount of volatilized ^{137}Cs exceeded the amount of volatized

436 ^{134}Cs by more than one order of magnitude.

437 The texture of FTB26 was highly porous with various submicron particles, such as silica
438 fibers, attached to the surface. Radioactive particles from Unit 1 (particle number CF-01-1) were
439 characterized in a previous study (Martin et al., 2020), although no glassy carbon core has been reported
440 for these particles. Martin et al. (2020) suggested that the core material of this particle was
441 aluminosilicate insulating material, although a significant carbon signal appeared in the SEM–EDX
442 spectrum scanned over the surfaces, which may be derived from a carbon coating or carbon core. In
443 their study, the carbon signal may have been missed because the hard incident X-rays in the synchrotron
444 facility arrive at very high energy (19 keV) (Martin et al., 2020). Thus, other Unit 1-derived particles
445 reported in previous studies might have contained a carbon core. After normalization with the
446 approximately calculated volume, the $^{134+137}$Cs activity of FTB26 was of the same order of magnitude
447 as the $^{134+137}$Cs activity of a recently reported particle (Martin et al., 2020): 6.0×10^8 Bq/cm^3 for FTB26
448 and 2.9×10^9 Bq/cm^3 for particle CF-01-1 in Martin et al. (2020). This finding supports our hypothesis
449 of similar $^{134+137}$Cs activity.

450

451 4.2. Aerosols embedded in the surface of FTB26 as a record of airborne particles during the H_2 explosion

The surfaces of the highly radioactive particles were not always associated with fine micro-particles. The FTB1 surface revealed no embedded micro-particles; whereas, FTB26 exhibited numerous micro-particles embedded into the surface of its glassy carbon core. These particles likely became attached and embedded into the surface at the time of the hydrogen explosion, indicating that they were airborne in the reactor building when the explosion occurred. Radioactive Cs was detected only on the surface of FTB26, implying two possible scenarios: (1) Cs was associated with airborne micro-particles that were subsequently embedded through the explosion, or (2) volatilized Cs was first absorbed onto structural materials and was then fractionated and driven into the core of the particle during the explosion. The main average composition of these airborne particles was Al, Si, S, Ca, Ti, Fe, and Na, with a few wt.% of K and Mg (Table 3a). Airborne particles of various phases were identified: fibrous aluminosilicates (Fig. 5c), possibly derived from insulating materials (Martin et al., 2017); Ca phase (Ca carbonate) (Fig. 8a), most likely derived from concrete materials; Fe–Zn oxides (Fig. 8b); Fe–Cr oxide, which is likely the composition of stainless steel; and Pb–(Sn) alloy with various Sn contents (0–40%), possibly originating from solder or plating. The alloy is known to melt above 183 °C. Its two phases, alpha and liquid, coexist between 183 and ~230 °C, and $Pb_{60}Sn_{40}$ alloy exists entirely in the liquid phase (Fecht, 1991). The Sn-rich and Pb-rich domains should have phase-separated

468 during the heating and rapid cooling processes within the damaged reactor building. These airborne
469 particles differ from the inclusions in CsMPs, such as nanoparticles of various fission fragments, which
470 probably formed inside the PCV and which represent the composition of the airborne particles (Furuki
471 et al., 2017; Imoto et al., 2017). Such a difference has two possible causes: the different sizes of the
472 micro-particles embedded in the FTB26 surface and the nano-particle inclusions within CsMPs, and the
473 different particle-formation processes at different locations in the reactor building (outside the PCV for
474 FTB26 and inside for CsMPs).
475
476 4.3. Significance of the new highly radioactive particles in the environment and their health impacts
477 The high $^{134+137}$Cs activity per particle (for FTB1 and FTB26) poses a potential threat to
478 health and the environment. Such high $^{134+137}$Cs activity per particle has never been reported in
479 Fukushima, and the health impacts have never been discussed, although "hot particles" derived from
480 nuclear reactor facilities in Europe have been serially reported. For instance, Charles and Harrison
481 (2007) determined the ^{137}Cs content of radioactive particles at the Dounreay nuclear site in Scotland
482 (10^3–10^8 Bq) and estimated the external and internal exposures to the human body through inhalation,
483 ingestion, and skin contact (Charles and Harrison, 2007). The external dose from a fuel fragment

484 emitting 10^5 Bq of ^{137}Cs is extremely small at some distance from the particle, even when no radiation
485 shielding is installed. Therefore, the highly radioactive particles in the area contaminated by Unit 1 are
486 unlikely to cause acute health effects through external exposure. Regarding inhalation, particles of size
487 <10 μm can reach the deep lung tissue and increase the risk of lung cancer, whereas particles of size
488 >10 μm can deposit higher in the respiratory tract without reaching the bronchi (Charles and Harrison,
489 2007). Because both FTB1 and FTB26 characterized in this study are too large to reach the respiratory
490 tract, the effects of inhalation are ignored. From a regression curve (Charles and Harrison, 2007), the
491 external-radiation dose rates of FTB1 and FTB26 with ^{137}Cs activities of ~10^5 and ~10^6 Bq respectively
492 were estimated as 0.3 and 2–4 Gy h^{-1}, respectively (averaged over 1 cm^2 at a distance of 70 μm from
493 the skin surface). As the threshold for skin damage is ~2 Gy (NRPB, 1997), stationary contact with
494 particles such as FTB26 (emitting ~10^6 Bq ^{137}Cs) can potentially cause skin lesions within 0.5–1.0 h.
495 However, dry particles sized >50 μm do not typically adhere to dry skin (Sheppard, 1994), so the skin
496 damage caused by the highly radioactive particles is considered to be minimal. In addition, the ingested
497 dose of particles with ~10^5 Bq ^{137}Cs activity was previously estimated as 10–20 mGy (Charles, 2009;
498 Charles and Harrison, 2007), three orders of magnitude lower than the estimated threshold dose of lethal
499 damage to the colon (Stather et al., 1988). Comparing the new highly radioactive particles with the

500 particles reported in previous studies, the human health effects of the highly radioactive particles
501 discovered in the present study can be regarded as negligible. The effects of highly radioactive particles
502 on the other living organisms, such as filter feeders, may however be of particular concern due to their
503 size and high activity, and as such this may warrant further study for FDNPP impacted environments.
504 Indeed, a previous experimental study exposing a highly radioactive particle derived from the Dounreay
505 reactor site (UK) (dose rate of ~3 Gy/h; ~10^5 Bq of ^{137}Cs) to the marine mollusc *Mytilus edulis,*
506 demonstrated increased DNA damage and necrosis in the mollusc's mantle tissue (Jaeschke et al., 2015).
507 Another study has also reported that a freshwater mussel, *Limnoperna fortunei*, accumulated radioactive
508 Cs released from FDNPP and the biological half-life was calculated to be much longer than the typical
509 biological half-life of Cs (Matsuzaki et al., 2014).
510 The high $^{134+137}$Cs activity of FTB1 and FTB26 could also influence the transfer of the
511 radiation dose through the ambient environment (when placed 1 cm from the particles, the scintillation
512 survey meters of FTB1 and FTB26 read ~1 and >5 μSv/h, respectively). In addition, the $^{134+137}$Cs
513 activities of both particles exceeded the bulk $^{134+137}$Cs activity per unit mass of soil samples (KU-536 =
514 1.65×10^4 Bq/g) excluding the highly radioactive particles (Table S1). This indicates that the occurrence
515 and mobility of such particles could greatly influence the local radiation dose. Therefore, removing

516 these particles would effectively reduce the ambient radiation dose in the area impacted by Unit 1. In
517 addition, the occurrence of highly radioactive particles in shallow aquatic environments (rivers and
518 ponds) would influence the distribution coefficient, K_d, of radioactive Cs between solids and waters;
519 that is, the excess amount of radioactive Cs could be distributed to the solid fraction, which would
520 impact models for radioactive Cs migration (for example, as reported in a previous study: Konoplev et
521 al., 2016).
522
523 4.4. Implications of radioactive particles released during meltdowns
524 As with other radioactive particles, such as CsMPs and Unit 1-derived particles, highly
525 radioactive particles can be rigorously characterized to better understand the conditions inside the
526 nuclear reactor building during meltdown. In particular, FTB26 records the composition of the airborne
527 particles in the reactor building at the moment of H_2 explosion. This "frozen" explosion evidence is
528 valuable for elucidating the progression of catastrophic events in the reactor building, because such
529 information is lost or disturbed during subsequent events. The radioactive particles formed inside the
530 power plant are frequently associated with submicron- and nano-scale inclusions. Thus, besides posing
531 a potential thread of environmental and biological impacts, radioactive particles are an important

recording medium of the phenomena inside the power plant. Such information is crucial when particles are released from “ground zero”, where the extremely high radiation field blocks access to the site. This information can be retrieved from particles that are sparingly soluble in ambient environments, such as those characterized in our present and previous studies (Furuki et al., 2017; Imoto et al., 2017; Ochiai et al., 2018).

Acknowledgements

The authors are grateful to Dr. Watanabe for her assistance on SEM analyses at the Center of Advanced Instrumental Analysis, Kyushu University. This study is partially supported by JST Initiatives for Atomic Energy Basic and Generic Strategic Research and by a Grant-in-Aid for Scientific Research (KAKENHI) from the Japan Society for the Promotion of Science (16K12585, 16H04634, No. JP26257402). The findings and conclusions of the authors of this paper do not necessarily state or reflect those of the JST. We thank Diamond Light Source for beamtime NT21246-9, U.K.

CRediT authorship contribution statement

Kazuya Morooka: Formal analysis, Data curation, Writing – original draft. Eitaro Kurihara: Formal analysis. Masato Takehara: Formal analysis. Ryu Takami: Formal analysis. Kenij Horie: Formal analysis. Shinya Yamasaki: Investigation. Toshihiko Ohnuki: Resources. Bernd Grambow: Data curation, Writing – original draft. Gareth T.W. Law: Writing – original draft. Joyce W. L. Ang: Writing – original draft, Formal analysis. William R Bower: Formal analysis. Rodney C Ewing: Writing – original draft. Satoshi Utsunomiya: Conceptualization, Investigation, Writing – original draft.

560 **Figure captions**

561 **Figure 1.** Maps showing the location of Fukushima Daiichi Nuclear Power Plant (FDNPP) and sampling
562 sites on the map of $^{134+137}$Cs activity. Red filled circles indicate the locations of the present samples. The
563 red star represents the location of the soil sample containing FTB1 and FTB26. This map was modified
564 with permission from the Extension Site of Distribution Map of Radiation Dose/GSI Maps.

565

566 **Figure 2.** ^{134}Cs/^{137}Cs activity ratio versus ^{137}Cs activity. Filled red circles indicate the radioactive
567 particles isolated in the present study. Green, red and blue dotted lines represent the ^{134}Cs/^{137}Cs activity
568 ratios in Units 1, 2, and 3, respectively, at the time of the accident. For comparison, the ^{134}Cs/^{137}Cs
569 activity ratios of CsMPs reported in previous studies (Furuki et al., 2017; Imoto et al., 2017; Kurihara
570 et al., 2020; Ochiai et al., 2018; Suetake et al., 2019) are plotted for comparison. The green triangle
571 indicates the highest $^{134+137}$Cs activity and the ^{134}Cs/^{137}Cs activity ratio reported in radioactive particles
572 released from the FDNPP (Martin et al., 2020).

573

574 **Figure 3.** (a) Secondary electron (SE) image of FTB1 prior to crushing, accompanied by EDX elemental
575 maps of the major elements; (b) EDX spectrum of the area indicated by the yellow labels in the SE

images; (c) and (d) enlarged SE images. White arrows indicate smaller micro-particles adhered to the surface.

Figure 4. (a) HAADF–STEM image of the FIB–TEM specimen of FTB1-A associated with the elemental maps. The FIB sampling position is shown in the supporting information (Fig. S4). SAED pattern of flaky nanoparticles within the matrix. EDX spectra were collected from the areas indicated by the yellow labels in the HAADF–STEM image. (b) HAADEF–STEM image of FIB–TEM specimen of FTB1-B associated with the elemental maps and the SAED pattern of the matrix. EDX spectra of EDX3 and EDX4 are also shown.

Figure 5. (a) Secondary electron (SE) image of FTB26, (b) enlarged SE image of the surface of FTB26 associated with the elemental maps of its major constituents, (c) SE image of the fibrous structure of the FTB26 surface, and (d) EDX spectra of the points indicated by the yellow crosses in (b) and (c). Note that only EDX3 was obtained after SIMS analysis and coated with Au.

Figure 6. (a) X-ray fluorescence spectroscopy elemental mapping of FTB26, along with the optical

592 image. The contrast of the maps does not correspond to the concentration of each element but reveals
593 the heterogeneous distribution of each element within the particle. (b) A captured image of the three-
594 dimensional X-ray tomography image of FTB26 at the position of the sliced surface, and three sliced
595 images in different planes. The colors indicate the relative densities of components within the particle.
596 A movie is given in the supplementary material (movie S1).
597
598 **Figure 7.** (a) Back-scattered electron (BSE) image of the cross section of FTB26 (prepared by mounting
599 in epoxy resin and polishing), accompanied by elemental maps of its major constituents. (b) EDX
600 spectra: EDX1 collected from the area in the core enclosed by the yellow-edged square, and EDX2
601 averaged over the entire particle collected from the area enclosed by the yellow-dotted line. (c) A BSE
602 image enlarging the area outlined by the yellow-dotted square in (a) accompanied by elemental maps of
603 the major constituents
604
605 **Figure 8.** SEM analyses of individual micro-particles embedded within the carbon-core surface: (a)
606 BSE image showing the phases (*e.g.,* Pb-rich phase) of the micro-particles associated with the elemental
607 maps and the EDX spectra of the individual particles labeled EDX1–6 in the BSE image. (b) SE image

608 of micro-particles in the rim of FTB26 and an enlarged SE image of the area enclosed by the yellow-
609 dotted square in (a), along with the elemental maps of the major elements. EDX7–EDX9 are the EDX
610 spectra of three areas enclosed by the yellow-edged squares in the two SE images. (c) BSE image
611 showing a relatively large micro-particle fragment embedded in the surface, accompanied by the EDX
612 spectrum (EDX10) of the area enclosed by the yellow-edged square in that image. (d) SE image of a
613 micro-particle enriched in Pb only, and the EDX spectrum (EDX11) of the point indicated by the yellow
614 cross in that image. (e) BSE image of a large fractured micro-particle embedded in another part of the
615 rim, accompanied with the elemental maps of its major elements and the EDX spectrum of the entire
616 fragment outlined by the yellow dotted lines. (f) SE image of another rim part near a pore, accompanied
617 by elemental maps and the EDX spectrum (EDX13) of the point indicated by the yellow cross in that
618 image.
619
620 **Figure 9.** (a) HAADF–STEM image of the FIB specimen prepared from the carbon core at the cross
621 section of FTB26. The insert is a SAED pattern obtained from the area enclosed by the yellow-edged
622 circle in the HAADF image. (b) STEM–EDX spectrum of the area indicated by the yellow-edged square
623 in (a). (c) Electron energy-loss spectrum (EELS) of the C K-edge collected from the thin area.

624

625 **Figure 10.** (a) Reflective light micrograph of the cross section of FTB26. Red labels indicate the

626 positions of the SIMS analysis. (b)−(e) Isotope ratios of at the spots indicated by the red numbers in (a):

627 (b) mass-135 ($^{135}Cs + ^{135}Ba$) to ^{133}Cs, (c) mass-137 ($^{137}Cs + ^{137}Ba$) to ^{133}Cs, (d) mass-134 ($^{134}Cs + ^{134}Ba$)

628 to ^{138}Ba, and (e) mass-135 ($^{135}Cs + ^{135}Ba$) to mass-137 ($^{137}Cs + ^{137}Ba$). The green lines in (b)−(e) are the

629 ratios calculated in Unit 1 of the FDNPP (Nishihara et al., 2012), plotted for comparison.

630

631

632

633

634

635

636

637

638

639

640 **Reference**

641 Auvinen, A., Lehtinen, K.E.J., Enriquez, J., Jokiniemi, J.K., Zilliacus, R., 2000. Vaporisation rates of
642 CsOH and CsI in conditions simulating a severe nuclear accident. J. Aerosol Sci. 31, 1029–1043.
643 https://doi.org/10.1016/S0021-8502(00)00027-6

644 Buesseler, K., Dai, M., Aoyama, M., Benitez-Nelson, C., Charmasson, S., Higley, K., Maderich, V.,
645 Masqué, P., Morris, P.J., Oughton, D., Smith, J.N., 2017. Fukushima Daiichi–derived radionuclides
646 in the ocean: transport, fate, and impacts. Ann. Rev. Mar. Sci., Annual Review of Marine Science 9,
647 173–203. https://doi.org/10.1146/annurev-marine-010816-060733

648 Byrnes, I., Lind, O.C., Hansen, E.L., Janssens, K., Salbu, B., 2020. Characterization of radioactive particles
649 from the Dounreay nuclear reprocessing facility. Sci. Total Environ. 727, 138488.
650 https://doi.org/10.1016/j.scitotenv.2020.138488

651 Charles, M.W., 2009. Health Effects of Dounreay Hot Particles: A Benchmark for the Evaluation of Doses
652 and Risks, in: Radioactive Particles in the Environment. pp. 235–248. https://doi.org/10.1007/978-90-
653 481-2949-2_16

654 Charles, M.W., Harrison, J.D., 2007. Hot particle dosimetry and radiobiology—past and present. J. Radiol.
655 Prot. 27, A97–A109. https://doi.org/10.1088/0952-4746/27/3A/S11

656 Chino, M., Nakayama, H., Nagai, H., Terada, H., Katata, G., Yamazawa, H., 2011. Preliminary Estimation
657 of Release Amounts of 131 I and 137 Cs Accidentally Discharged from the Fukushima Daiichi
658 Nuclear Power Plant into the Atmosphere. J. Nucl. Sci. Technol. 48, 1129–1134.
659 https://doi.org/10.1080/18811248.2011.9711799
660 Eriksson, M., Osán, J., Jernström, J., Wegrzynek, D., Simon, R., Chinea-Cano, E., Markowicz, A.,
661 Bamford, S., Tamborini, G., Török, S., Falkenberg, G., Alsecz, A., Dahlgaard, H., Wobrauschek, P.,
662 Streli, C., Zoeger, N., Betti, M., 2005. Source term identification of environmental radioactive Pu/U
663 particles by their characterization with non-destructive spectrochemical analytical techniques.
664 Spectrochim. Acta Part B At. Spectrosc. 60, 455–469. https://doi.org/10.1016/J.SAB.2005.02.023
665 Eugster, O., Tera, F., Wasserburg, G.J., 1969. Isotopic analyses of barium in meteorites and in terrestrial
666 samples. J. Geophys. Res. 74, 3897–3908. https://doi.org/10.1029/JB074i015p03897
667 Fecht, H.J., 1991. Phase selection during crystallization of undercooled liquid eutectic lead-tin alloys. Acta
668 Metall. Mater. 39, 1003–1009. https://doi.org/10.1016/0956-7151(91)90301-G
669 Filik, J., Ashton, A.W., Chang, P.C.Y., Chater, P.A., Day, S.J., Drakopoulos, M., Gerring, M.W., Hart,
670 M.L., Magdysyuk, O. V., Michalik, S., Smith, A., Tang, C.C., Terrill, N.J., Wharmby, M.T.,
671 Wilhelm, H., 2017. Processing two-dimensional X-ray diffraction and small-angle scattering data in

672 DAWN 2. J. Appl. Crystallogr. 50, 959–966. https://doi.org/10.1107/S1600576717004708

673 Foster, G.L., Lécuyer, C., Marschall, H.R., 2016. Boron Stable Isotopes. pp. 1–6.

674 https://doi.org/10.1007/978-3-319-39193-9_238-1

675 Furuki, G., Imoto, J., Ochiai, A., Yamasaki, S., Nanba, K., Ohnuki, T., Grambow, B., Ewing, R.C.,

676 Utsunomiya, S., 2017. Caesium-rich micro-particles: A window into the meltdown events at the

677 Fukushima Daiichi Nuclear Power Plant. Sci. Rep. 7, 42731. https://doi.org/10.1038/srep42731

678 Hans Wedepohl, K., 1995. The composition of the continental crust. Geochim. Cosmochim. Acta 59, 1217–

679 1232. https://doi.org/10.1016/0016-7037(95)00038-2

680 IAEA, 2015. Technical Volume 1 of 5: Description and Context of the Accident, The Fukushima Daiichi

681 Accident. Vienna, Austria.

682 IAEA, 2011. Radioactive particles in the Environment: Sources, Particle Characterization and Analytical

683 Techniques. IAEA in Austria, Vienna, Austria.

684 Ikehara, R., Morooka, K., Suetake, M., Komiya, T., Kurihara, E., Takehara, Masato, Takami, R., Kino, C.,

685 Horie, K., Takehara, Mami, Yamasaki, S., Ohnuki, T., Law, G.T.W., Bower, W., Grambow, B.,

686 Ewing, R.C., Utsunomiya, S., 2020. Abundance and distribution of radioactive cesium-rich

687 microparticles released from the Fukushima Daiichi Nuclear Power Plant into the environment.

688 Chemosphere 241, 125019. https://doi.org/10.1016/j.chemosphere.2019.125019

689 Ikehara, R., Suetake, M., Komiya, T., Furuki, G., Ochiai, A., Yamasaki, S., Bower, W.R., Law, G.T.W.,

690 Ohnuki, T., Grambow, B., Ewing, R.C., Utsunomiya, S., 2018. Novel Method of Quantifying

691 Radioactive Cesium-Rich Microparticles (CsMPs) in the Environment from the Fukushima Daiichi

692 Nuclear Power Plant. Environ. Sci. Technol. 52, 6390–6398. https://doi.org/10.1021/acs.est.7b06693

693 Ikenoue, T., Takehara, M., Morooka, K., Kurihara, E., Takami, R., Ishii, N., Kudo, N., Utsunomiya, S.,

694 2020. Occurrence of highly radioactive microparticles in the seafloor sediment from the pacific coast

695 35 km northeast of the Fukushima Daiichi nuclear power plant. Chemosphere 128907.

696 https://doi.org/10.1016/j.chemosphere.2020.128907

697 Imoto, J., Ochiai, A., Furuki, G., Suetake, M., Ikehara, R., Horie, K., Takehara, M., Yamasaki, S., Nanba,

698 K., Ohnuki, T., Law, G.T.W., Grambow, B., Ewing, R.C., Utsunomiya, S., 2017. Isotopic signature

699 and nano-texture of cesium-rich micro-particles: Release of uranium and fission products from the

700 Fukushima Daiichi Nuclear Power Plant. Sci. Rep. 7, 5409. https://doi.org/10.1038/s41598-017-

701 05910-z

702 Iwata, H., Shiotsu, H., Kaneko, M., Utsunomiy, S., 2012a. Nuclear Accidents in Fukushima, Japan, and

703 Exploration of Effective Decontaminant for the 137Cs-Contaminated Soils, in: Advances in Nuclear

Fuel. InTech. https://doi.org/10.5772/33540

Iwata, H., Shiotsu, H., Kaneko, M., Utsunomiya, S., 2012b. Nuclear Accidents inFukushima, Japan, and Exploration of Effictive Decontaminant for the 137Cs-Contaminated Soils, in: Revankar, S. (Ed.), ADVANCES IN NUCLEAR FUEL. INTECH, pp. 123–174.

Jaeschke, B.C., Lind, O.C., Bradshaw, C., Salbu, B., 2015. Retention of radioactive particles and associated effects in the filter-feeding marine mollusc Mytilus edulis. Sci. Total Environ. 502, 1–7. https://doi.org/10.1016/j.scitotenv.2014.09.007

Kaneko, M., Iwata, H., Shiotsu, H., Masaki, S., Kawamoto, Y., Yamasaki, S., Nakamatsu, Y., Imoto, J., Furuki, G., Ochiai, A., Nanba, K., Ohnuki, T., Ewing, R.C., Utsunomiya, S., 2015. Radioactive Cs in the Severely Contaminated Soils Near the Fukushima Daiichi Nuclear Power Plant. Front. Energy Res. 3, 37. https://doi.org/10.3389/fenrg.2015.00037

Katata, G., Terada, H., Nagai, H., Chino, M., 2012. Numerical reconstruction of high dose rate zones due to the Fukushima Dai-ichi Nuclear Power Plant accident. J. Environ. Radioact. 111, 2–12. https://doi.org/10.1016/j.jenvrad.2011.09.011

Konoplev, A., Golosov, V., Laptev, G., Nanba, K., Onda, Y., Takase, T., Wakiyama, Y., Yoshimura, K., 2016. Behavior of accidentally released radiocesium in soil–water environment: Looking at

720 Fukushima from a Chernobyl perspective. J. Environ. Radioact. 151, 568–578.
721 https://doi.org/10.1016/j.jenvrad.2015.06.019
722 Koo, Y.-H., Yang, Y.-S., Song, K.-W., 2014. Radioactivity release from the Fukushima accident and its
723 consequences: A review. Prog. Nucl. Energy 74, 61–70.
724 https://doi.org/10.1016/j.pnucene.2014.02.013
725 Kurihara, E., Takehara, Masato, Suetake, M., Ikehara, R., Komiya, T., Morooka, K., Takami, R.,
726 Yamasaki, S., Ohnuki, T., Horie, K., Takehara, Mami, Law, G.T.W., Bower, W., W. Mosselmans,
727 J.F., Warnicke, P., Grambow, B., Ewing, R.C., Utsunomiya, S., 2020. Particulate plutonium released
728 from the Fukushima Daiichi meltdowns. Sci. Total Environ. 743, 140539.
729 https://doi.org/10.1016/j.scitotenv.2020.140539
730 Marchal, J., Horswell, I., Willis, B., Plackett, R., Gimenez, E.N., Spiers, J., Ballard, D., Booker, P.,
731 Thompson, J.A., Gibbons, P., Burge, S.R., Nicholls, T., Lipp, J., Tartoni, N., 2013. EXCALIBUR: a
732 small-pixel photon counting area detector for coherent X-ray diffraction - Front-end design,
733 fabrication and characterisation. J. Phys. Conf. Ser. 425, 062003. https://doi.org/10.1088/1742-
734 6596/425/6/062003
735 Martin, P.G., Jones, C.P., Cipiccia, S., Batey, D.J., Hallam, K.R., Satou, Y., Griffiths, I., Rau, C., Richards,

736 D.A., Sueki, K., Ishii, T., Scott, T.B., 2020. Compositional and structural analysis of Fukushima-
737 derived particulates using high-resolution x-ray imaging and synchrotron characterisation techniques.
738 Sci. Rep. 10, 1636. https://doi.org/10.1038/s41598-020-58545-y
739 Martin, P.G., Louvel, M., Cipiccia, S., Jones, C.P., Batey, D.J., Hallam, K.R., Yang, I.A.X., Satou, Y., Rau,
740 C., Mosselmans, J.F.W., Richards, D.A., Scott, T.B., 2019. Provenance of uranium particulate
741 contained within Fukushima Daiichi Nuclear Power Plant Unit 1 ejecta material. Nat. Commun. 1–7.
742 https://doi.org/10.1038/s41467-019-10937-z
743 Martin, P.G., Satou, Y., Griffiths, I., Richards, D., Scott, T., 2017. Analysis of External Surface
744 Irregularities on Fukushima-Derived Fallout Particles. Front. Energy Res. 5.
745 https://doi.org/10.3389/fenrg.2017.00025
746 Matsuzaki, S.S., Satake, K., Tanaka, A., Ueno, R., Nakagawa, M., Nohara, S., 2014. The fate,
747 concentration factors and ecological half-life of cesium-137 in a freshwater snail and a freshwater
748 mussel in Lake Kasumigaura after the Fukushima Nuclear Accident. Japanese J. Limnol.
749 (Rikusuigaku Zasshi) 76, 25–34. https://doi.org/10.3739/rikusui.76.25
750 Miwa, S., Takase, G., Imoto, J., Nishioka, S., Miyahara, N., Osaka, M., 2020. Boron chemistry during
751 transportation in the high temperature region of a boiling water reactor under severe accident

conditions. J. Nucl. Sci. Technol. 57, 291–300. https://doi.org/10.1080/00223131.2019.1671913

Miwa, S., Yamashita, S., Osaka, M., 2016. Prediction of the effects of boron release kinetics on the vapor species of cesium and iodine fission products. Prog. Nucl. Energy 92, 254–259. https://doi.org/10.1016/j.pnucene.2016.02.023

Nakajima, T., Misawa, S., Morino, Y., Tsuruta, H., Goto, D., Uchida, J., Takemura, T., Ohara, T., Oura, Y., Ebihara, M., Satoh, M., 2017. Model depiction of the atmospheric flows of radioactive cesium emitted from the Fukushima Daiichi Nuclear Power Station accident. Prog. Earth Planet. Sci. 4, 2. https://doi.org/10.1186/s40645-017-0117-x

Nishihara, K., Iwamoto, H., Suyama, K., 2012. Estimation of fuel compositions in Fukushima-Daiichi Nuclear Power Plant, JAEA Technical Report. Japan Atomic Energy Agency, JAEA 2012-018, Ibaraki, Japan.

Nomura, A., 1969. Fukushima Nuclear Power Station, Tokyo Electric Power Co. J. At. Energy Soc. Japan / At. Energy Soc. Japan 11, 306–314. https://doi.org/10.3327/jaesj.11.306

NRPB, 1997. Assessment of skin doses, Volume 8, No.3. Chilton, UK.

Ochiai, A., Imoto, J., Suetake, M., Komiya, T., Furuki, G., Ikehara, R., Yamasaki, S., Law, G.T.W., Ohnuki, T., Grambow, B., Ewing, R.C., Utsunomiya, S., 2018. Uranium Dioxides and Debris

768 Fragments Released to the Environment with Cesium-Rich Microparticles from the Fukushima
769 Daiichi Nuclear Power Plant. Environ. Sci. Technol. 52, 2586–2594.
770 https://doi.org/10.1021/acs.est.7b06309
771 Ono, T., Yushin, I., Abe, Y., Nakai, I., Terada, Y., Satou, Y., Sueki, K., Adachi, K., Igarashi, Y., 2017.
772 Investigation of the Chemical Characteristics of Individual Radioactive Microparticles Emitted from
773 Reactor 1 by the Fukushima Daiichi Nuclear Power Plant Accident by Using Multiple Synchrotron
774 Radiation X-ray Analyses. Bunseki Kagaku 66, 251–261.
775 https://doi.org/10.2116/bunsekikagaku.66.251
776 Pontillon, Y., Ducros, G., Malgouyres, P.P., 2010. Behaviour of fission products under severe PWR
777 accident conditions VERCORS experimental programme—Part 1: General description of the
778 programme. Nucl. Eng. Des. 240, 1843–1852. https://doi.org/10.1016/j.nucengdes.2009.06.028
779 Salbu, B., Krekling, T., Lind, O.C., Oughton, D.H., Drakopoulos, M., Simionovici, A., Snigireva, I.,
780 Snigirev, A., Weitkamp, T., Adams, F., Janssens, K., Kashparov, V.A., 2001. High energy X-ray
781 microscopy for characterisation of fuel particles. Nucl. Instruments Methods Phys. Res. Sect. A
782 Accel. Spectrometers, Detect. Assoc. Equip. 467–468, 1249–1252. https://doi.org/10.1016/S0168-
783 9002(01)00641-6

784 Satou, Y., Sueki, K., Sasa, K., Yoshikawa, H., Nakama, S., Minowa, H., Abe, Y., Nakai, I., Ono, T.,
785 Adachi, K., Igarashi, Y., 2018. Analysis of two forms of radioactive particles emitted during the early
786 stages of the Fukushima Dai-ichi Nuclear Power Station accident. Geochem. J. 52, 1–7.
787 https://doi.org/10.2343/geochemj.2.0514
788 Sheppard, S.C., 1994. Contaminant Enrichment and Properties of Soil Adhering to Skin. J. Environ. Qual.
789 604–613. https://doi.org/10.2134/jeq1994.00472425002300030029x
790 Solé, V.A., Papillon, E., Cotte, M., Walter, P., Susini, J., 2007. A multiplatform code for the analysis of
791 energy-dispersive X-ray fluorescence spectra. Spectrochim. Acta Part B At. Spectrosc. 62, 63–68.
792 https://doi.org/10.1016/j.sab.2006.12.002
793 Stather, J.W., Muirhead, C.R., Edwards, A.A., Harrison, J.D., Lloyd, D.C., Wood, N.R., 1988. Health
794 effects models developed from the 1988 UNSCEAR report, NRPB-R-226. Chilton, UK.
795 Steinhauser, G., Brandl, A., Johnson, T.E., 2014. Comparison of the Chernobyl and Fukushima nuclear
796 accidents: A review of the environmental impacts. Sci. Total Environ. 470–471, 800–817.
797 https://doi.org/10.1016/j.scitotenv.2013.10.029
798 Suetake, M., Nakano, Y., Furuki, G., Ikehara, R., Komiya, T., Kurihara, E., Morooka, K., Yamasaki, S.,
799 Ohnuki, T., Horie, K., Takehara, M., Law, G.T.W., Bower, W., Grambow, B., Ewing, R.C.,

800 Utsunomiya, S., 2019. Dissolution of radioactive, cesium-rich microparticles released from the
801 Fukushima Daiichi Nuclear Power Plant in simulated lung fluid, pure-water, and seawater.
802 Chemosphere. https://doi.org/10.1016/j.chemosphere.2019.05.248
803 TEPCO, 2017. The 5th Progress Report on the Investigation and Examination of Unconfirmed and
804 Unresolved Issues on the Development Mechanism of the Fukushima Daiichi Nuclear Accident.
805 Tsuruta, H., Oura, Y., Ebihara, M., Ohara, T., Nakajima, T., 2015. First retrieval of hourly atmospheric
806 radionuclides just after the Fukushima accident by analyzing filter-tapes of operational air pollution
807 monitoring stations. Sci. Rep. 4, 6717. https://doi.org/10.1038/srep06717
808 Utsunomiya, S., Furuki, G., Ochiai, A., Yamasaki, S., Nanba, K., Grambow, B., Ewing, R.C., 2019.
809 Caesium fallout in Tokyo on 15th March, 2011 is dominated by highly radioactive, caesium-rich
810 microparticles.
811 Yao, M., Xiao, J., Fan, X., Liu, R., Liu, B., 2014. Transparent, superhard amorphous carbon phase from
812 compressing glassy carbon. Appl. Phys. Lett. 104, 021916. https://doi.org/10.1063/1.4861929
813 Zeng, Z., Yang, L., Zeng, Q., Lou, H., Sheng, H., Wen, J., Miller, D.J., Meng, Y., Yang, W., Mao, W.L.,
814 Mao, H., 2017. Synthesis of quenchable amorphous diamond. Nat. Commun. 8, 322.
815 https://doi.org/10.1038/s41467-017-00395-w

816

Table 1. Decay-corrected activities (as of March 12, 2011) of ^{134}Cs and ^{137}Cs in FTB1 and FTB26. The standard deviations are given in parentheses.

Sample No.	^{137}Cs (Bq)	^{134}Cs (Bq)	Total activity (^{134}Cs + ^{137}Cs)	$^{134}Cs/^{137}Cs$ activity ratio
FTB1	3.10×10^5 (±92)	3.01×10^5 (±348)	6.11×10^5	0.971
FTB26	1.27×10^6 (±107)	1.21×10^6 (±543)	2.48×10^6	0.954

Table 2. Average composition of FTB1 (wt.%) based on semi-quantitative STEM–EDX analysis. Numbers in parentheses are the standard deviations.

wt %	MgO	Al_2O_3	SiO_2	K_2O	CaO	TiO_2	Fe_2O_3	Cs_2O
FTB1-A	0.30	29.10	68.38	0.05	0.09	0.35	0.98	0.83
n = 14	(±0.15)	(±0.80)	(±1.38)	(±0.02)	(±0.03)	(±0.77)	(±0.15)	(±0.31)
FTB1-B	0.19	27.46	70.51	0.07	0.09	0.09	0.95	0.68
n = 7	(±0.17)	(±2.81)	(±3.00)	(±0.02)	(±0.04)	(±0.04)	(±0.29)	(±0.15)

Table 3. Compositions (wt%) of (a) the whole FTB26 and (b) fine particles embedded in the FTB26 surface, based on semi-quantitative SEM–EDX analyses. *The elemental composition was calculated because of lack of oxygen in the EDX spectrum.

(a)

Na_2O	MgO	Al_2O_3	SiO_2	SO_3	K_2O	CaO	TiO_2	Fe_2O_3
5.79	2.49	8.62	44.5	10.9	1.29	8.90	8.41	9.09

(b)

Wt. %	Na_2O	MgO	Al_2O_3	SiO_2	PbO	SO_3	K_2O	CaO	TiO_2	Cr_2O_3	Fe_2O_3	CuO	ZnO	NiO	SnO_2
EDX1	2.75		0.61	4.19	4.63			1.34		8.72	71.28		4.60	1.87	
EDX2*					100										
EDX3								100							
EDX4	0.31	2.59	8.76	39.82				24.15			24.36				
EDX5				100											
EDX6	13.95	3.11	3.49	70.25				9.20							
EDX7			1.01	4.33	0.98			0.62			73.88		19.19		
EDX8*					55.72										44.28
EDX9		5.28	10.00	32.85		7.39		30.07			14.41				
EDX10	11.01	3.50	2.33	75.10				8.05							
EDX11*					100										
EDX12	2.12	2.75	17.14	53.94		2.79	1.86	5.76	3.31		7.13	1.77	1.42		
EDX13				100											

Table 4. (a) Summary of B-isotope analysis and quantification on the surface of FTB26. The B concentration was deduced by comparing the ion counts of FTB26 with those in the NIST standard SRM612. Numbers in parentheses are the standard deviations. Spot numbers correspond to those in Fig. S6c. (b) $^{11}B/^{10}B$ isotope ratio collected for the NIST standard reference material SRM612. The numbers in parentheses are the standard deviations of six scans.

(a)

Spot No.	$^{11}B/^{10}B$ isotopic ratio	B (ppm)
1	4.137 (±0.016)	3056
2	4.275 (±0.027)	246.6
3	4.196 (±0.015)	888.2
4	4.144 (±0.014)	6625
5	4.156 (±0.191)	5.322

(b)

	$^{11}B/^{10}B$ isotopic ratio (n=6)
SRM612	4.049 (±0.007)

Table 5. SIMS analysis results on the cross section of FTB26. (a) ^{133}Cs ion counts per second analyzed at spots No. 1–8 in Fig. 10a. (b) Ion-count ratios of masses 133, 134, 135, 137, and 138. All values are given with their standard deviations. Note that the ion-count ratios and isotope ratios are not equivalent, as Cs and Ba have different ionization efficiencies. The spot numbers correspond to the positions labeled in Fig. 10a.

Spot No.	^{133}Cs ions (cps)
1	1
2	1
3	17253
4	14336
5	19371
6	3599
7	8739
8	1443

(b)

Spot No.	^{135}(Cs+Ba)/^{133}Cs	^{137}(Cs+Ba)/^{133}Cs	^{134}(Cs+Ba)/^{138}Ba	^{135}(Cs+Ba)/^{137}(Cs+Ba)
3	1.0738 ± 0.0100	2.071 ± 0.0193	0.0371 ± 0.0001	0.5185 ± 0.0005
4	0.7469 ± 0.0027	1.5431 ± 0.0054	0.0397 ± 0.0001	0.4840 ± 0.0004
5	0.4902 ± 0.0019	0.9920 ± 0.0035	0.0442 ± 0.0004	0.4942 ± 0.0009
6	1.1826 ± 0.0236	2.2426 ± 0.0447	0.0367 ± 0.00004	0.5273 ± 0.0008
7	0.7855 ± 0.0154	1.5426 ± 0.0301	0.0390 ± 0.0001	0.5092 ± 0.0007
8	0.8223 ± 0.1084	1.6193 ± 0.2134	0.0410 ± 0.0003	0.5078 ± 0.0016

Figure

Click here to access/download;Figure;Morooka2020STOTEN Figure v9.pdf

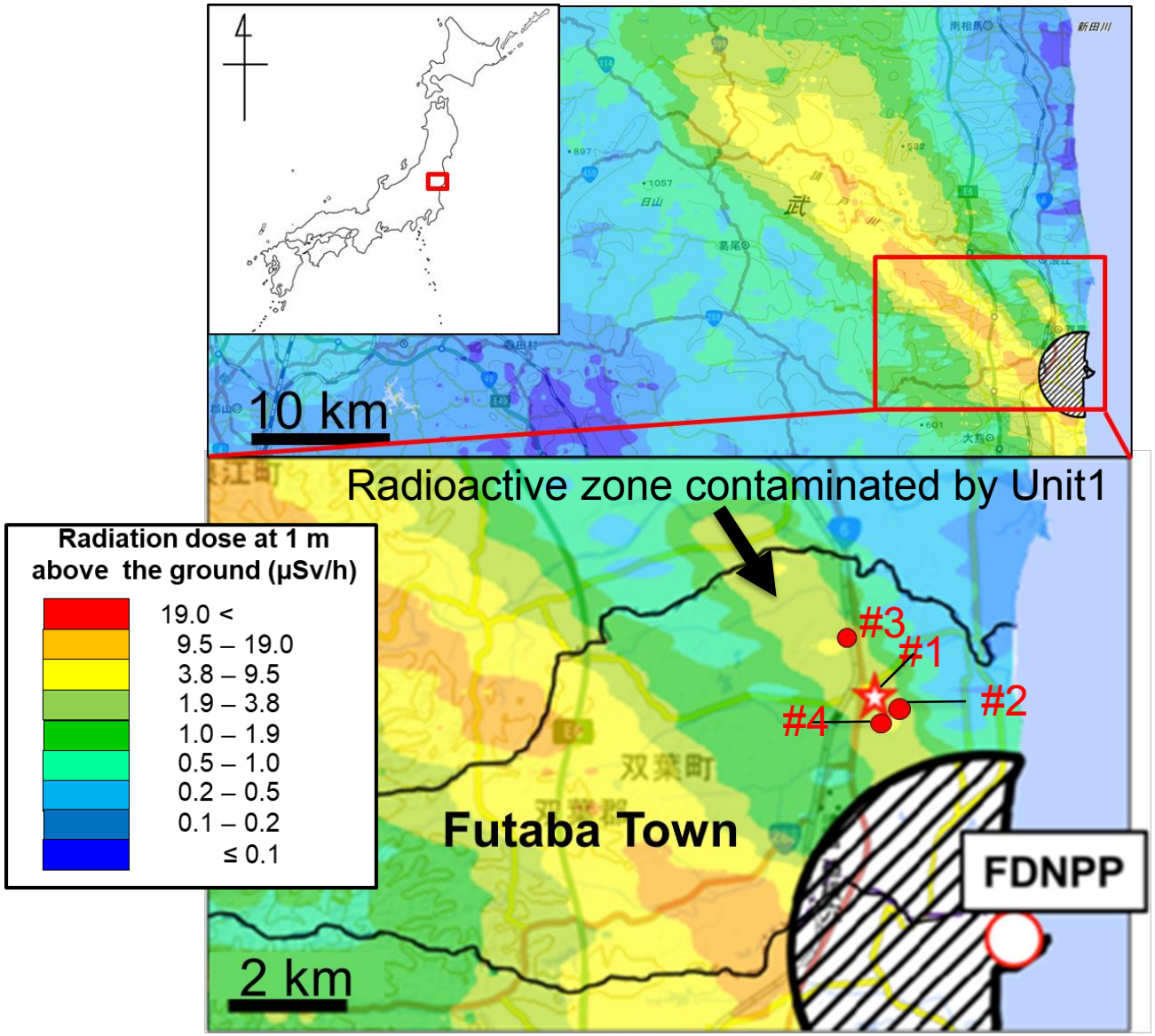

Fig.1

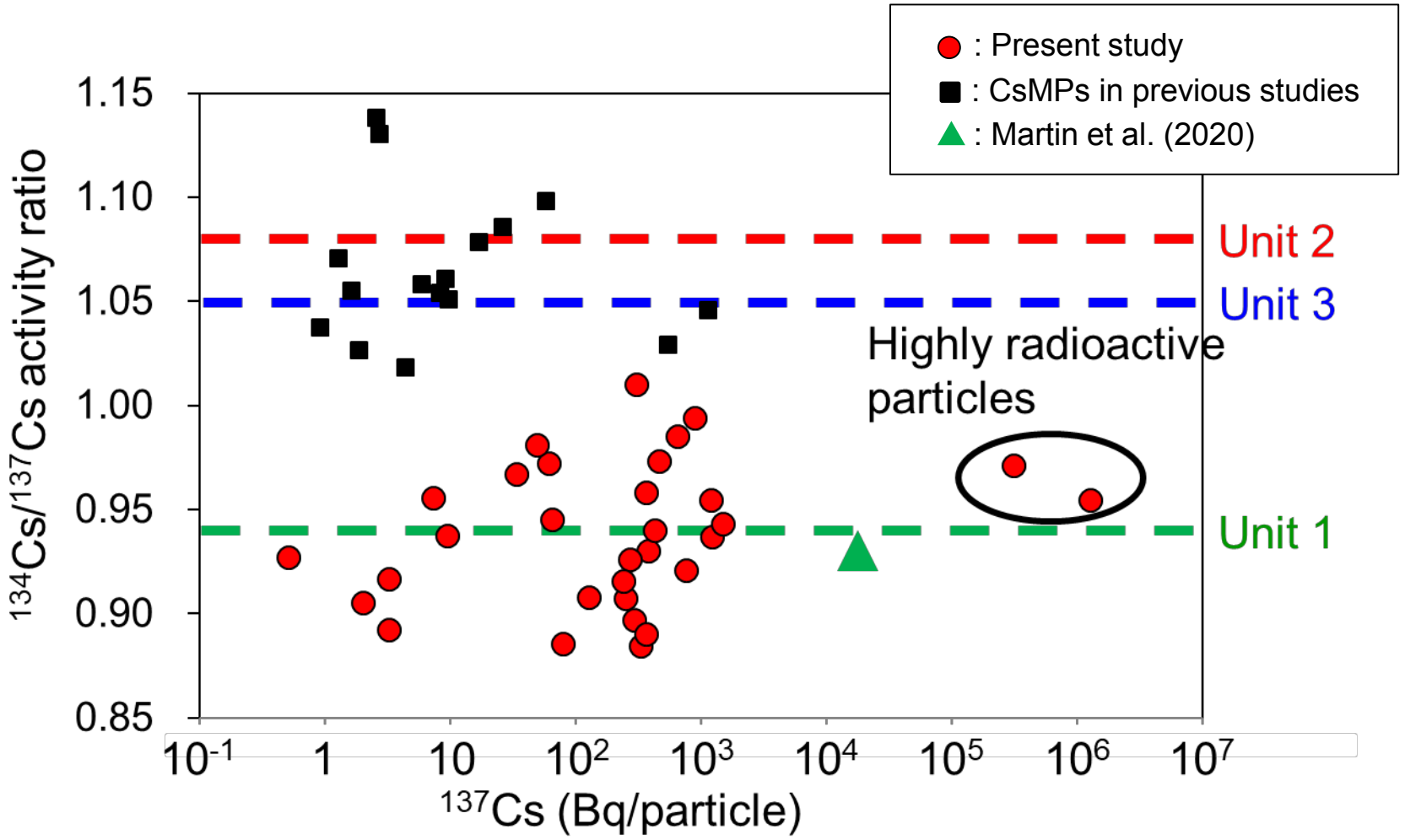
: Present study
: CsMPs in previous studies
: Martin et al. (2020)
Unit 2
Unit 3
Unit 1
Highly radioactive particles
1.15
1.10
1.05
1.00
0.95
0.90
0.85
$^{134}Cs/^{137}Cs$ activity ratio
10^{-1}
1
10
10^{2}
10^{3}
10^{4}
10^{5}
10^{6}
10^{7}
^{137}Cs (Bq/particle)

Fig.2

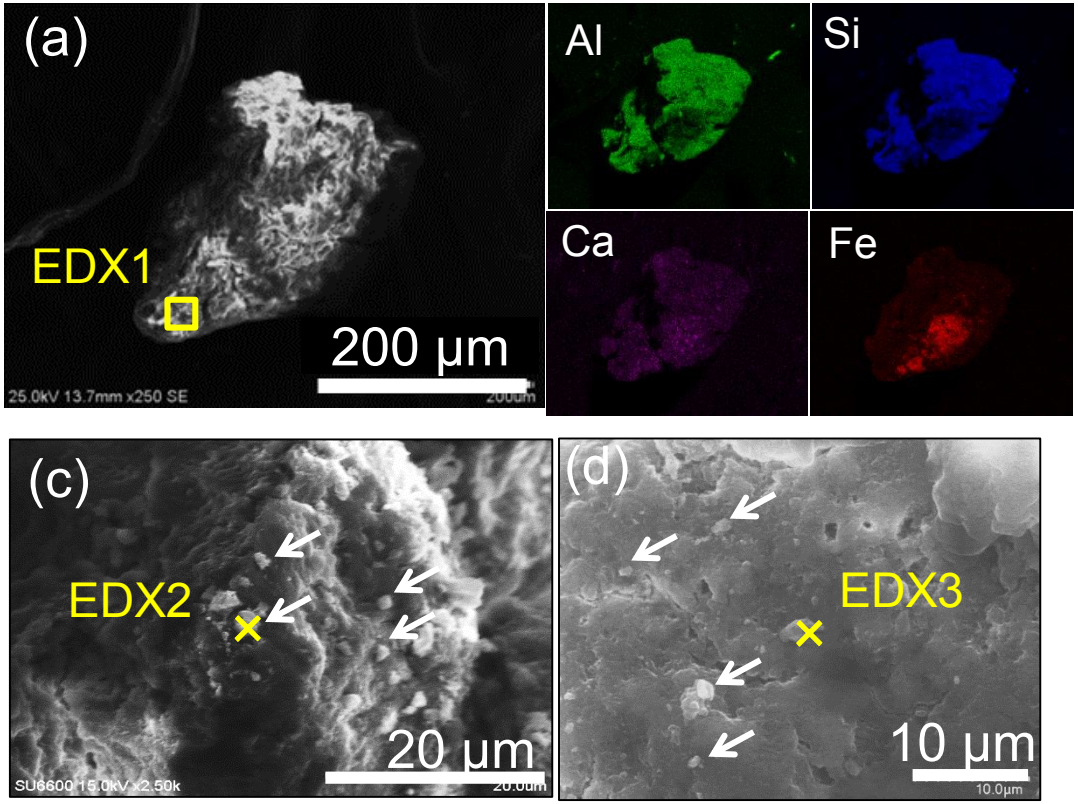
(a)
EDX1
200 μm
25.0kV 13.7mm x250 SE
Al
Si
Ca
Fe
(c)
EDX2
20 μm
SU6600 15.0kV x2.50k
(d)
EDX3
10 μm
10.0μm

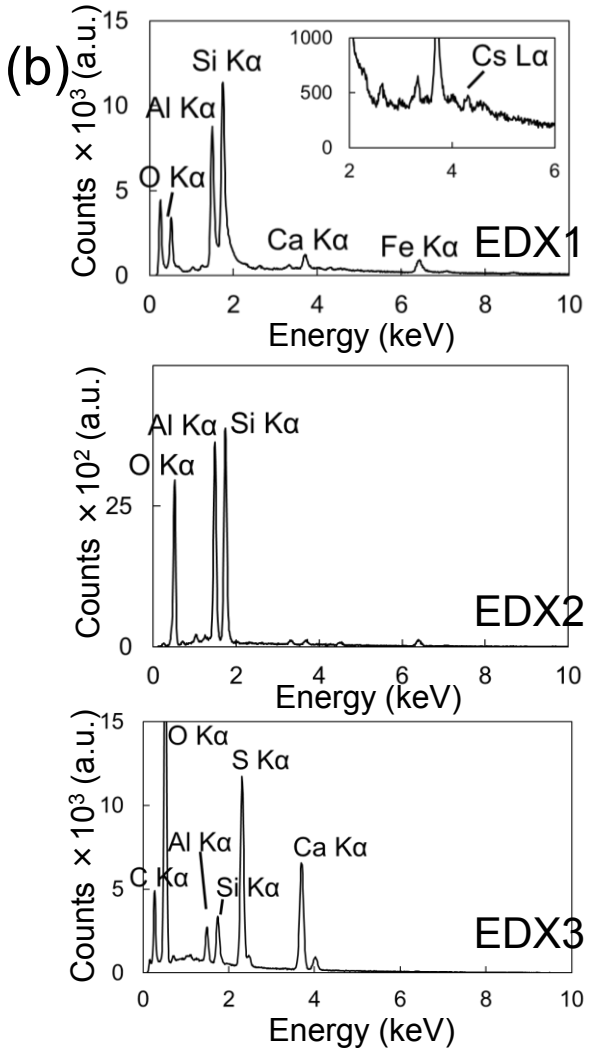
(b)
Counts × 10³ (a.u.)
Si Kα
Al Kα
O Kα
Ca Kα
Fe Kα
Cs Lα
EDX1
Energy (keV)
Counts × 10² (a.u.)
Al Kα
Si Kα
O Kα
EDX2
Energy (keV)
Counts × 10³ (a.u.)
O Kα
S Kα
Al Kα
Ca Kα
C Kα
Si Kα
EDX3
Energy (keV)

Fig.3

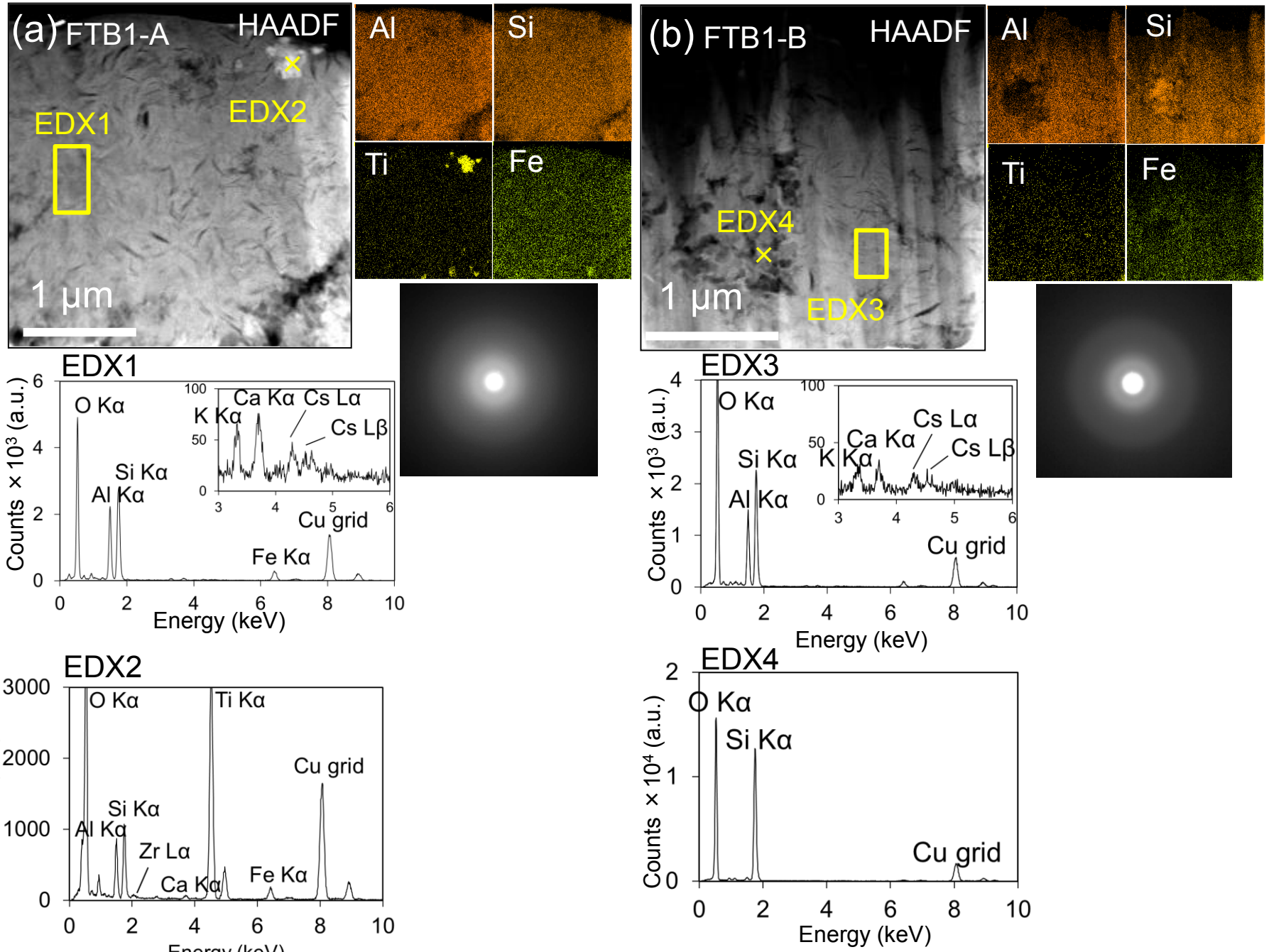
(a) FTB1-A
HAADF
EDX1
EDX2
1 μm
Al
Si
Ti
Fe
(b) FTB1-B
HAADF
EDX4
EDX3
1 μm
Al
Si
Ti
Fe
EDX1
Counts × 10³ (a.u.)
O Kα
Si Kα
Al Kα
K Kα
Ca Kα
Cs Lα
Cs Lβ
Cu grid
Fe Kα
Energy (keV)
EDX3
Counts × 10³ (a.u.)
O Kα
Si Kα
Al Kα
Ca Kα
K Kα
Cs Lα
Cs Lβ
Cu grid
Energy (keV)
EDX2
Counts (a.u.)
O Kα
Ti Kα
Cu grid
Si Kα
Al Kα
Zr Lα
Ca Kα
Fe Kα
Energy (keV)
EDX4
Counts × 10⁴ (a.u.)
O Kα
Si Kα
Cu grid
Energy (keV)

Fig.4

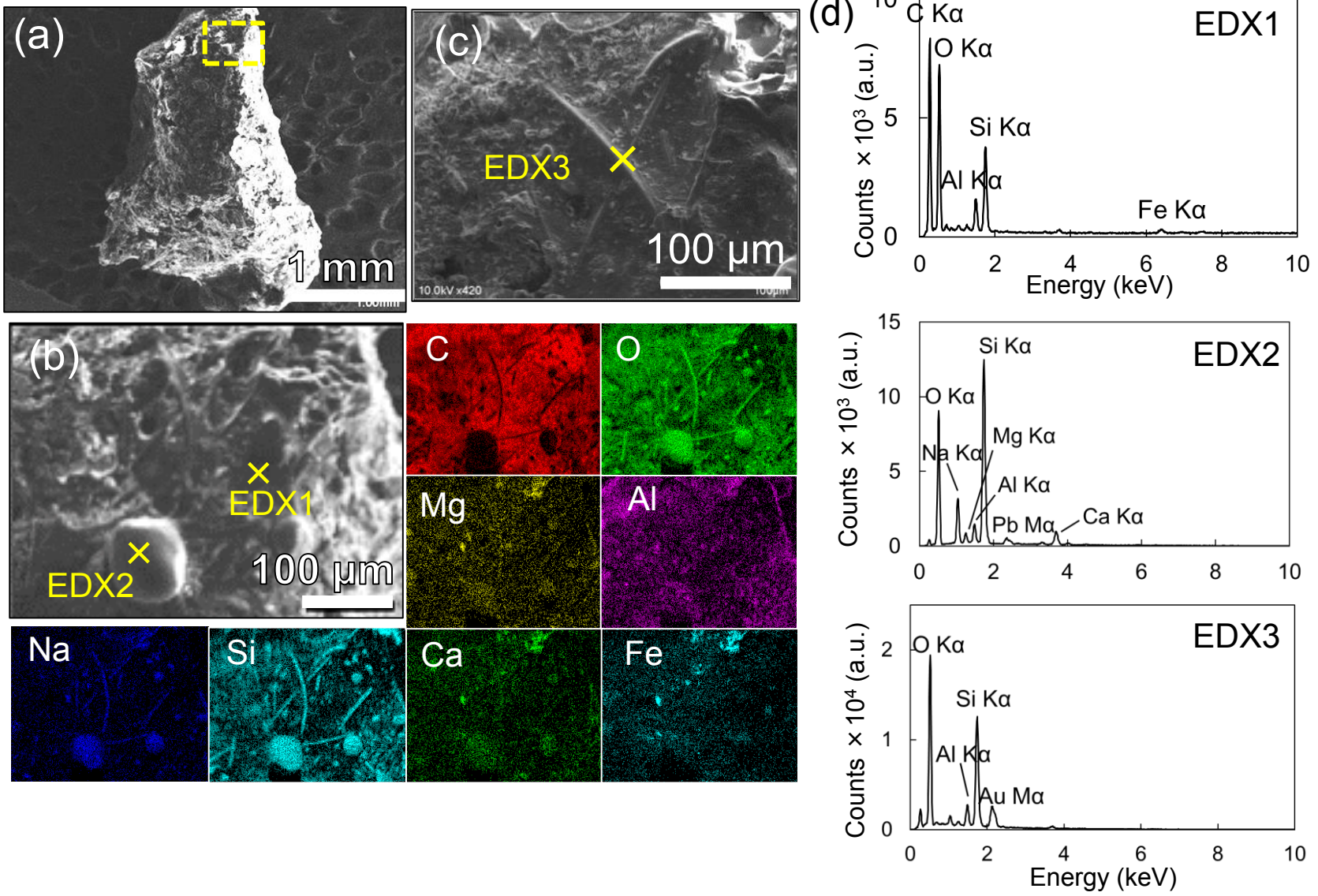
(a)
1 mm
(c)
EDX3
100 μm
(b)
EDX1
EDX2
100 μm
C
O
Mg
Al
Na
Si
Ca
Fe
(d)
EDX1
C Kα
O Kα
Si Kα
Al Kα
Fe Kα
Counts × 10³ (a.u.)
Energy (keV)
EDX2
Si Kα
O Kα
Mg Kα
Na Kα
Al Kα
Pb Mα
Ca Kα
Counts × 10³ (a.u.)
EDX3
O Kα
Si Kα
Al Kα
Au Mα
Counts × 10⁴ (a.u.)
Energy (keV)

Fig.5

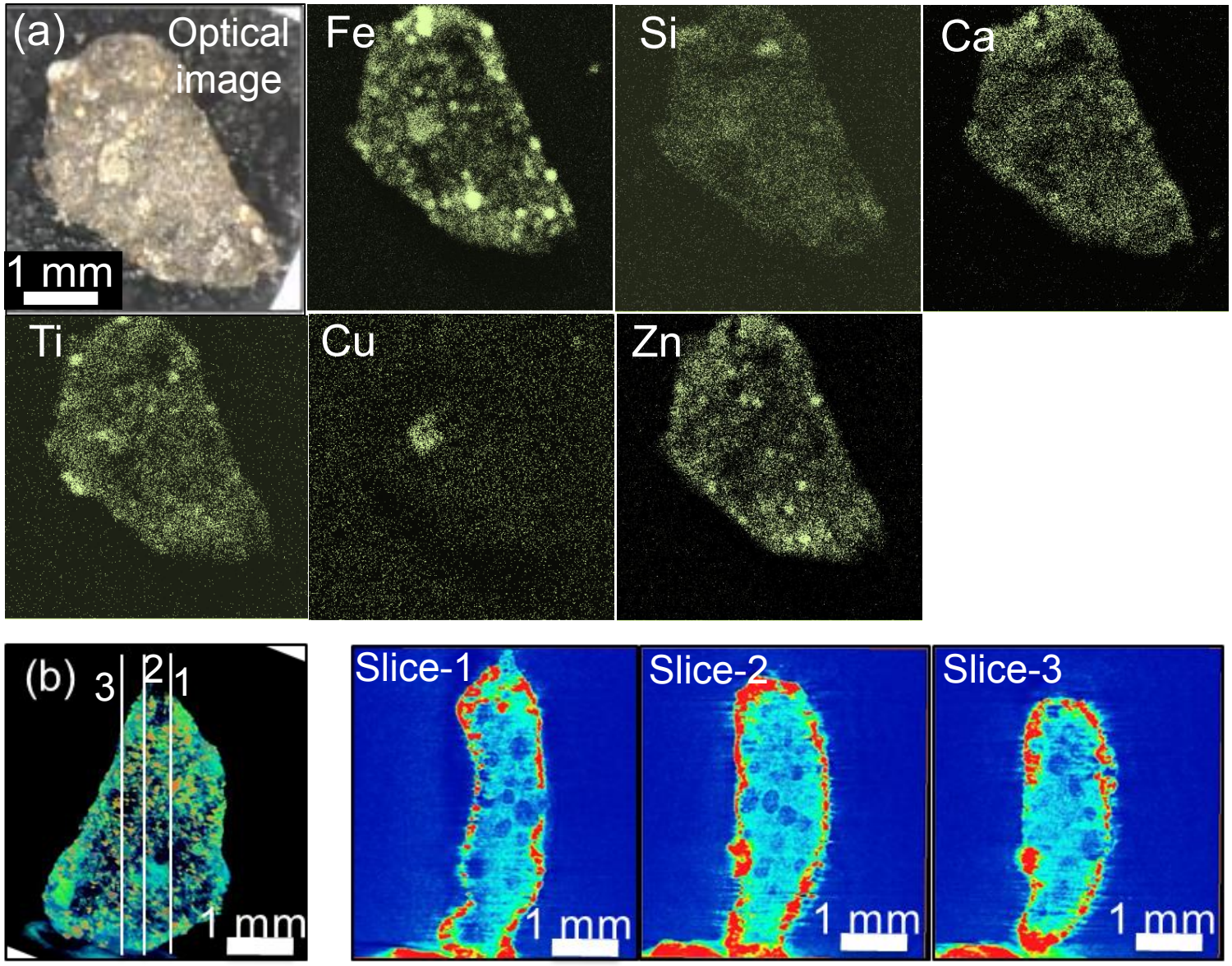
(a)
Optical image
1 mm
Fe
Si
Ca
Ti
Cu
Zn
(b)
3
2
1
1 mm
Slice-1
1 mm
Slice-2
1 mm
Slice-3
1 mm

Fig. 6

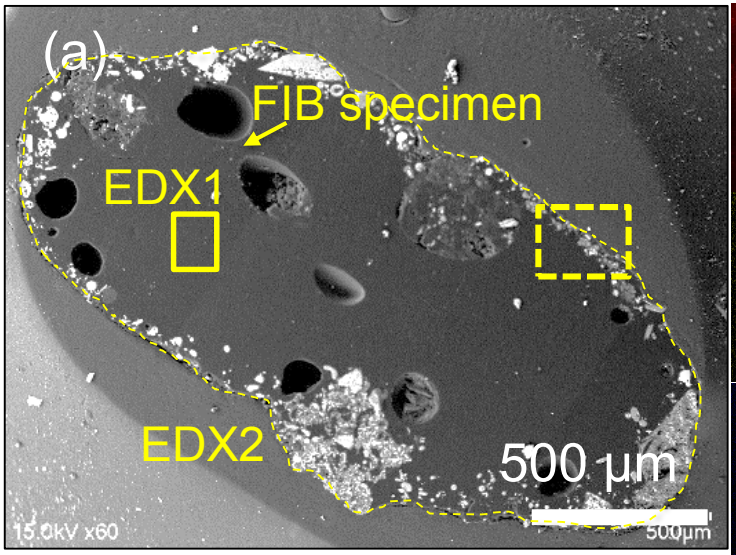
(a)
FIB specimen
EDX1
EDX2
500 μm
15.0kV x60
500μm

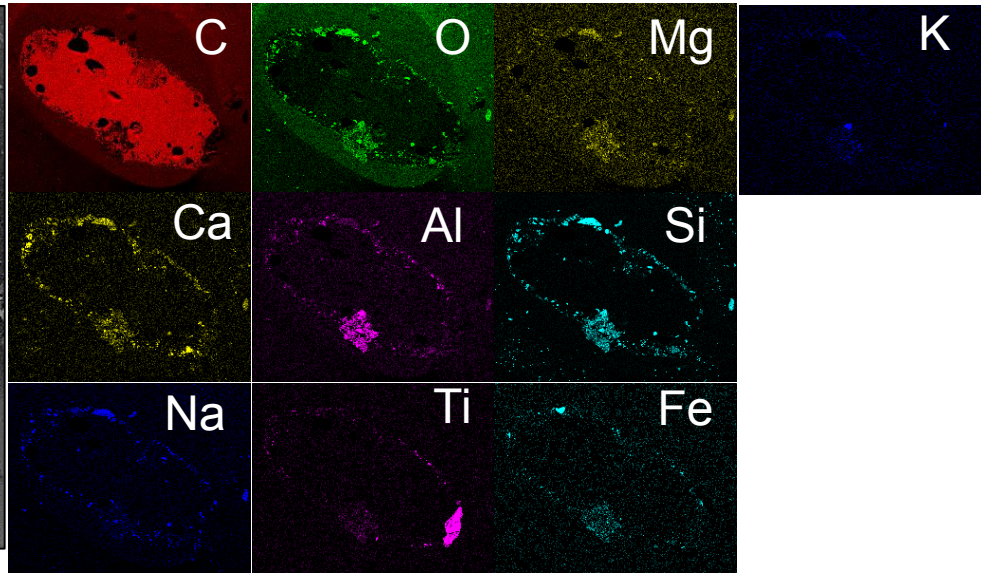
C
O
Mg
K
Ca
Al
Si
Na
Ti
Fe

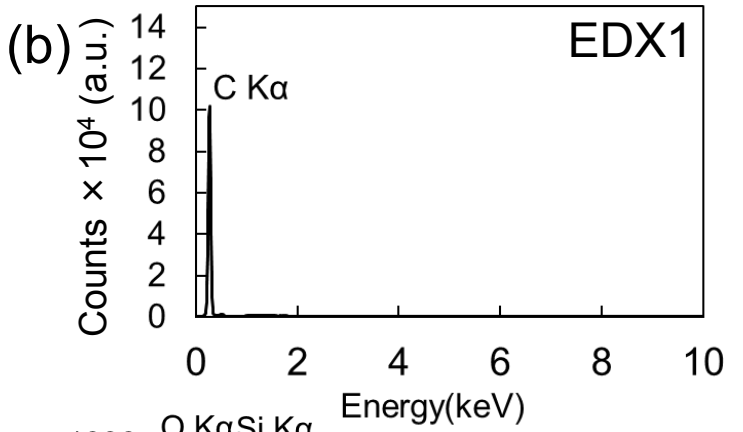
(b)
EDX1
Counts × 10⁴ (a.u.)
C Kα
Energy(keV)

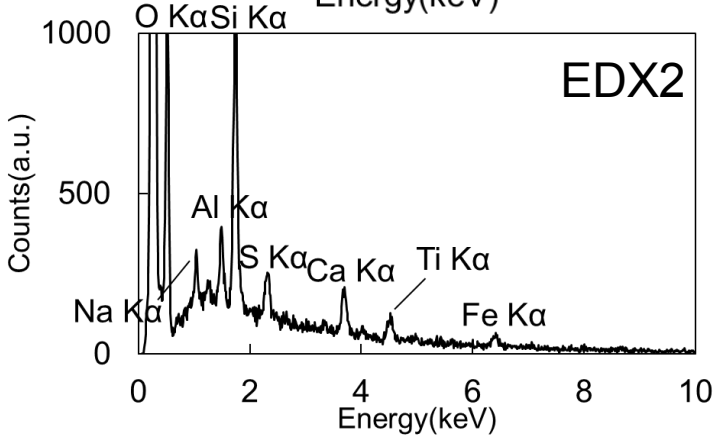
EDX2
Counts(a.u.)
O Kα
Si Kα
Al Kα
S Kα
Ca Kα
Ti Kα
Na Kα
Fe Kα
Energy(keV)

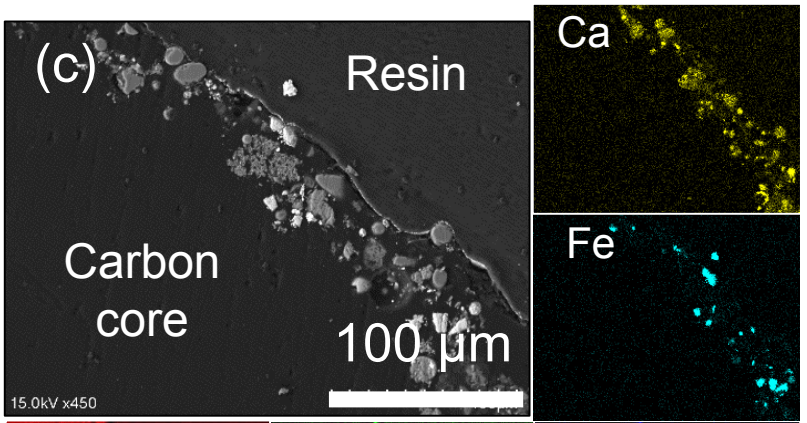
(c)
Resin
Carbon
core
100 μm
15.0kV x450

Ca
Fe

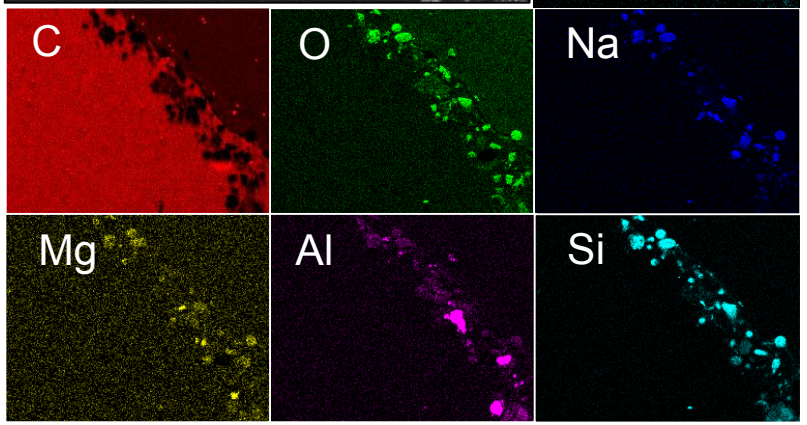
C
O
Na
Mg
Al
Si

Fig. 7

(a)

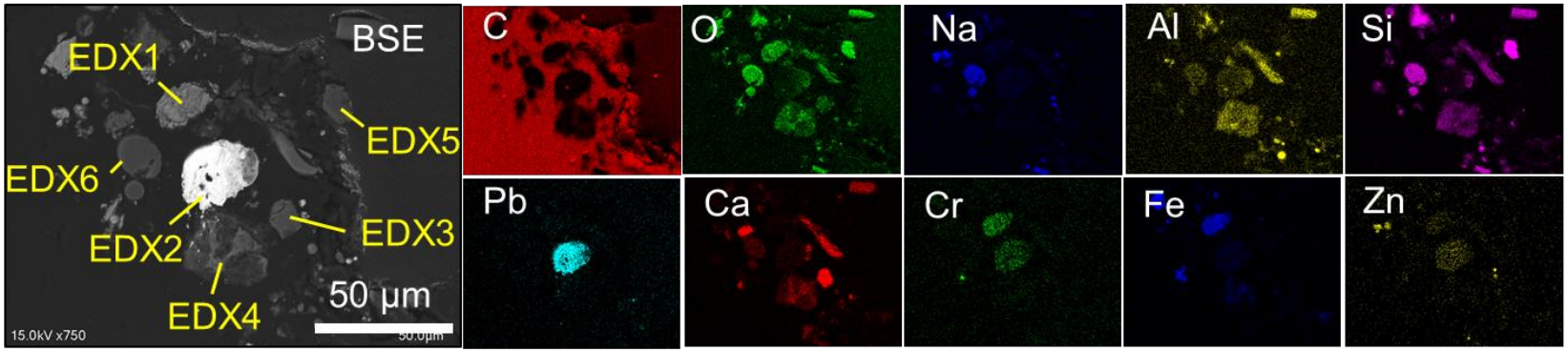
BSE
EDX1
EDX5
EDX6
EDX2
EDX3
EDX4
50 μm
15.0kV x750
C
O
Na
Al
Si
Pb
Ca
Cr
Fe
Zn

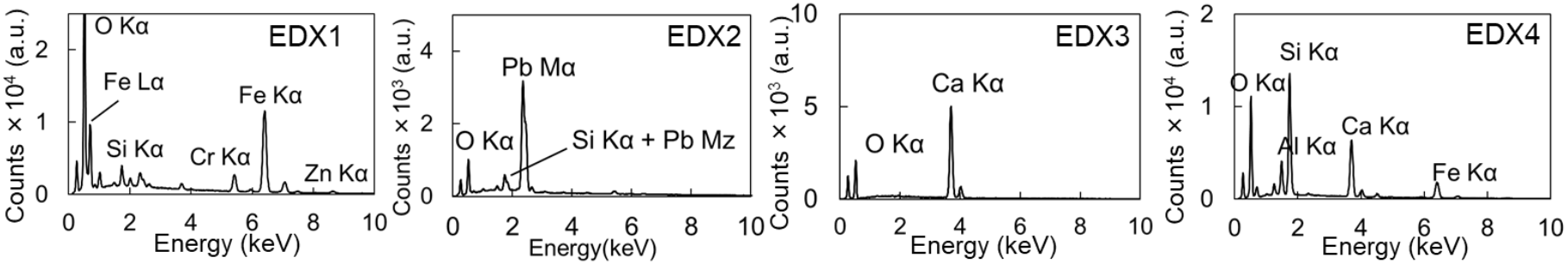
EDX1
O Kα
Fe Lα
Si Kα
Cr Kα
Fe Kα
Zn Kα
Counts × 10⁴ (a.u.)
Energy (keV)
EDX2
Pb Mα
O Kα
Si Kα + Pb Mz
Counts × 10³ (a.u.)
Energy(keV)
EDX3
Ca Kα
O Kα
Counts × 10³ (a.u.)
Energy (keV)
EDX4
Si Kα
O Kα
Al Kα
Ca Kα
Fe Kα
Counts × 10⁴ (a.u.)
Energy (keV)

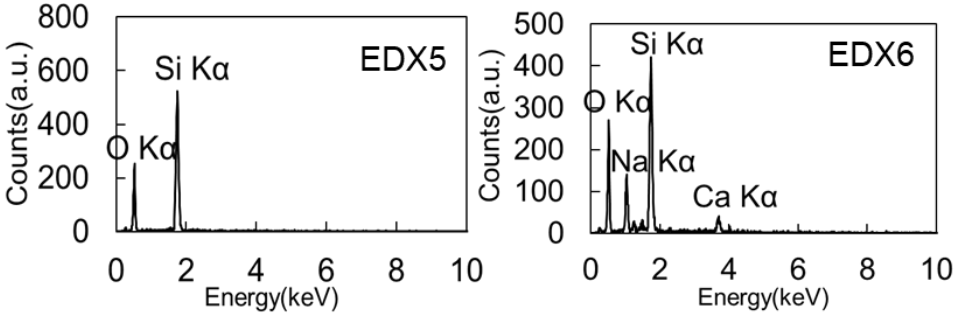
EDX5
Si Kα
O Kα
Counts(a.u.)
Energy(keV)
EDX6
Si Kα
O Kα
Na Kα
Ca Kα
Counts(a.u.)
Energy(keV)

Fig. 8

(b)

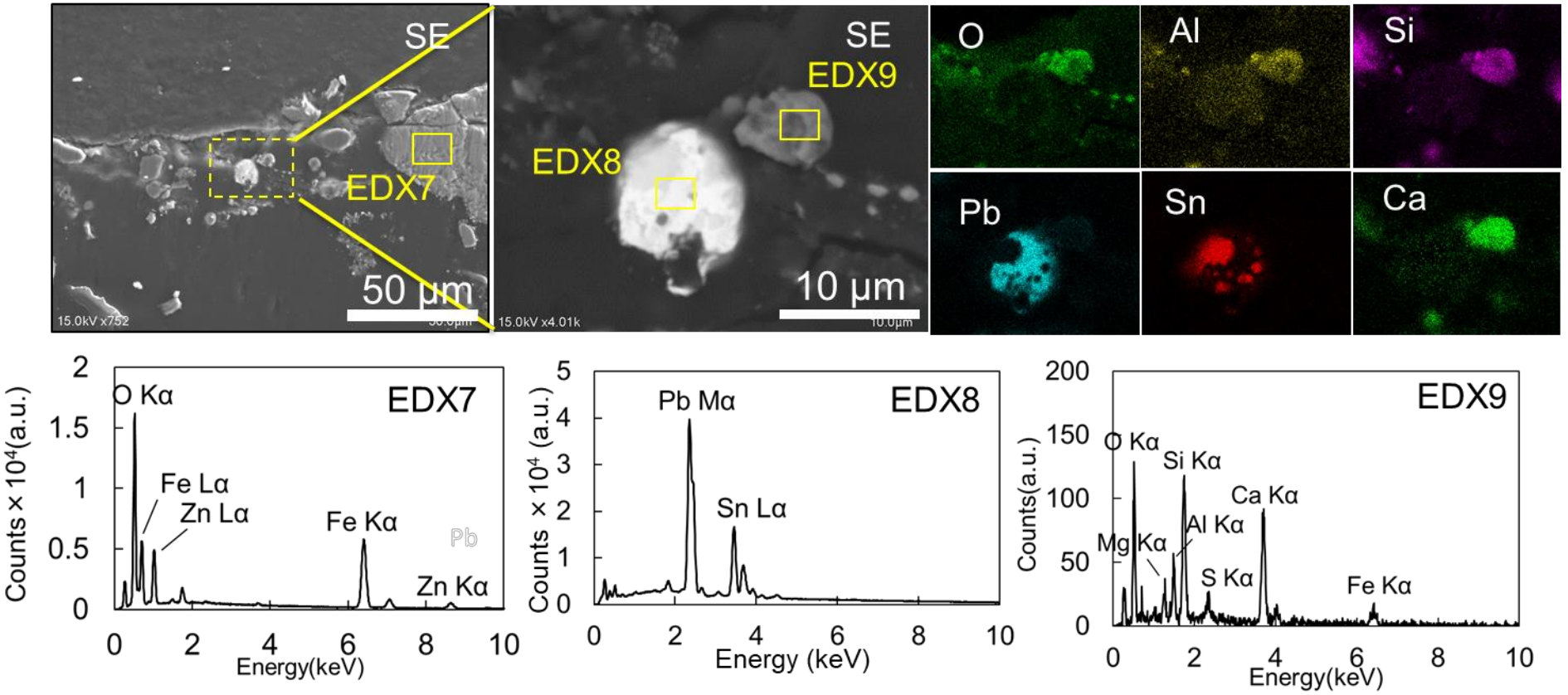

Fig. 8 (continued)

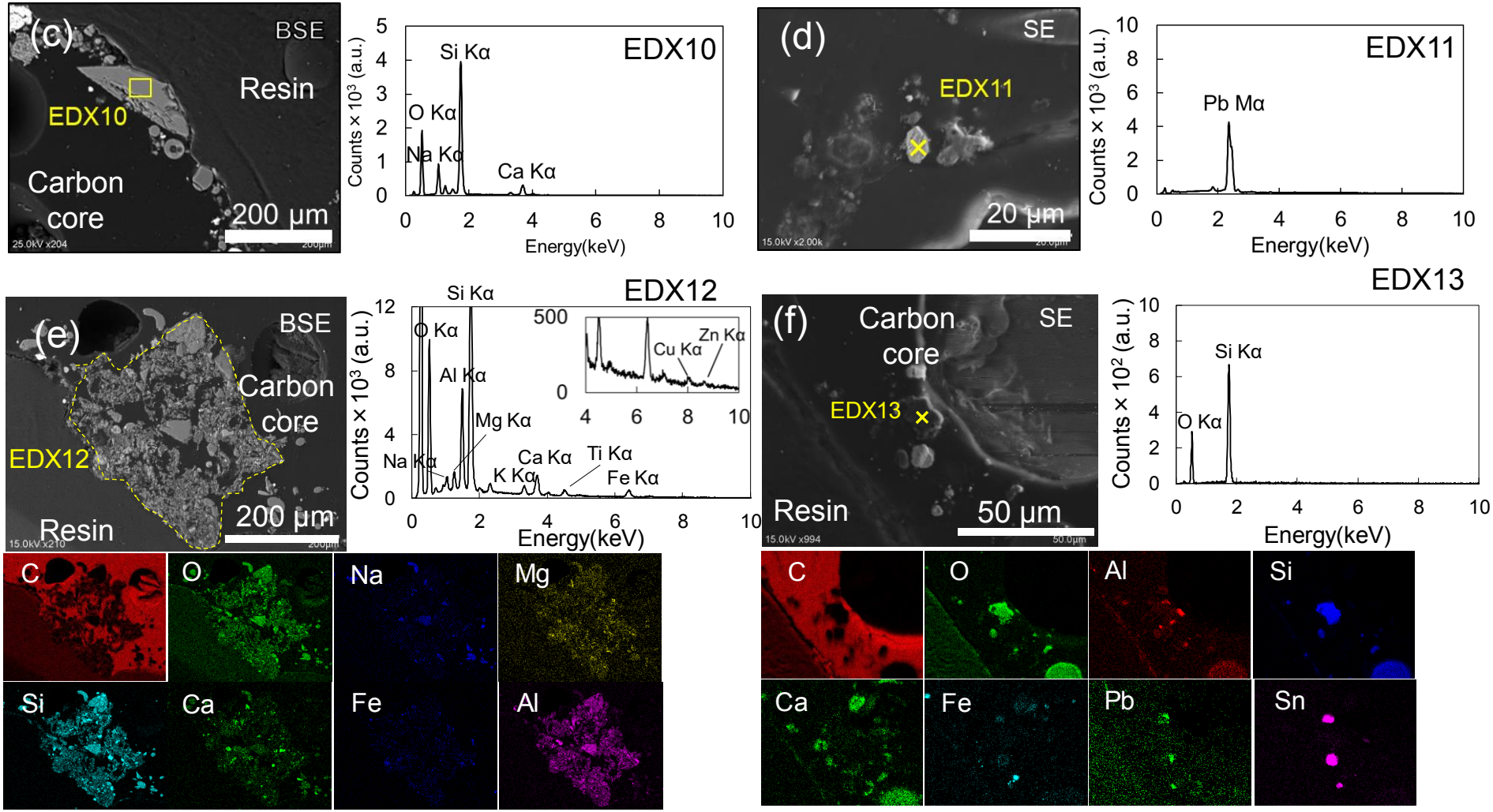

Fig. 8 (continued)

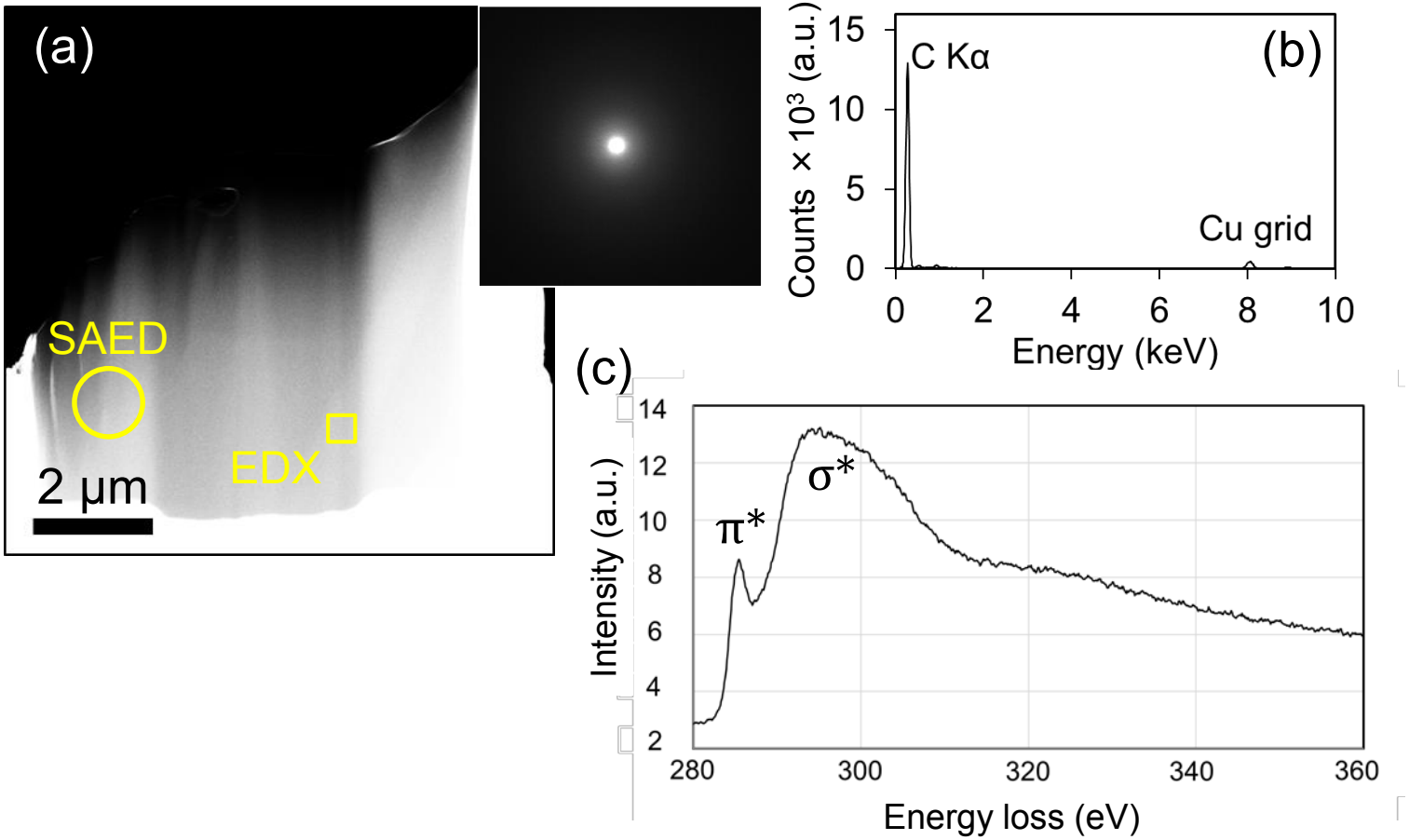
(a)
SAED
EDX
2 μm
(b)
C Kα
Cu grid
Counts × 10³ (a.u.)
Energy (keV)
(c)
π*
σ*
Intensity (a.u.)
Energy loss (eV)

Fig. 9

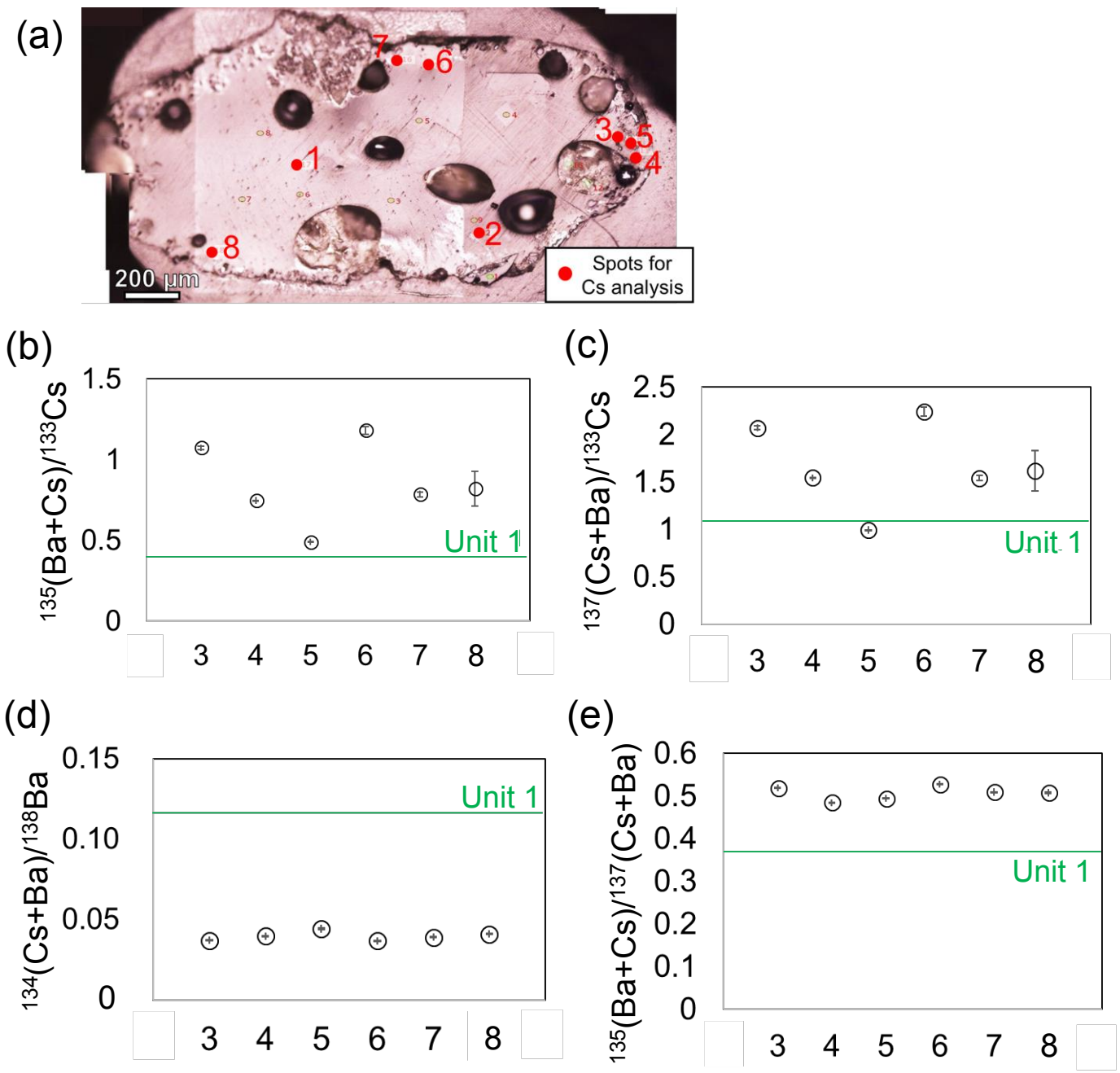
(a)
7
6
3
5
4
1
2
8
200 µm
Spots for Cs analysis
(b)
^{135}(Ba+Cs)/^{133}Cs
1.5
1
0.5
0
Unit 1
3 4 5 6 7 8
(c)
^{137}(Cs+Ba)/^{133}Cs
2.5
2
1.5
1
0.5
0
Unit 1
3 4 5 6 7 8
(d)
^{134}(Cs+Ba)/^{138}Ba
0.15
0.10
0.05
0
Unit 1
3 4 5 6 7 8
(e)
^{135}(Ba+Cs)/^{137}(Cs+Ba)
0.6
0.5
0.4
0.3
0.2
0.1
0
Unit 1
3 4 5 6 7 8

Fig. 10

Video

Click here to access/download

Video

Moroka2020STOTEN SI movie S1.avi

CRediT authorship contribution statement

Kazuya Morooka: Formal analysis, Data curation, Writing – original draft. Eitaro Kurihara: Formal analysis. Masato Takehara: Formal analysis. Ryu Takami: Formal analysis. Kenij Horie: Formal analysis. Shinya Yamasaki: Investigation. Toshihiko Ohnuki: Resources. Bernd Grambow: Data curation, Writing – original draft. Gareth T.W. Law: Writing – original draft. Joyce W. L. Ang: Writing – original draft, Formal analysis. William R Bower: Formal analysis. Rodney C Ewing: Writing – original draft. Satoshi Utsunomiya: Conceptualization, Investigation, Writing – original draft.